

The Near-Infrared Coronal Line Spectrum of 54 Nearby Active Galactic Nuclei

A. Rodríguez-Ardila

Laboratório Nacional de Astrofísica/MCT - Rua dos Estados Unidos 154, Bairro das Nações. CEP 37504-364, Itajubá, MG, Brazil

aardila@lna.br

M. A. Prieto

Instituto de Astrofísica de Canarias (IAC), C/Vía Láctea, s/n, E-38205, La Laguna, Tenerife, Spain

aprieto@iac.es

J. G. Portilla

Observatorio Astronómico Nacional, Facultad de Ciencias, Sede Bogotá, Universidad Nacional de Colombia

jgportillab@unal.edu.co

and

J. M. Tejeiro

Observatorio Astronómico Nacional, Facultad de Ciencias, Sede Bogotá, Universidad Nacional de Colombia

jmtejeiross@unal.edu.co

ABSTRACT

The relationship between emission of coronal lines (CLs) and nuclear activity in 36 Type 1 and 18 Type 2 active galactic nuclei (AGNs) is analyzed, for the first time, based on near infrared (0.8-2.4 μm) spectra. The eight CLs studied, of Si, S, Fe, Al and Ca elements and corresponding to ionization potentials (IP) in the range 125 – 450 eV, are detected (3σ) in 67% (36 AGNs) of the sample. Our analysis show that the four most frequent coronal lines [Si VI] 1.963 μm , [S VIII] 0.9913 μm , [S IX] 1.252 μm and [Si X] 1.430 μm , display a narrow range in

luminosity, with most lines located in the interval $\log L$ 39 - 40 ergs^{-1} . We found that the non-detection is largely associated with either a loss of spatial resolution or increasing object distance: CLs are essentially nuclear and easily lose contrast in the continuum stellar light for nearby sources or get diluted by the strong AGN continuum as the redshift increases. Yet, there are AGNs where the lack of coronal emission, i.e., lines with $IP \geq 100$ eV, may be genuine. The absence of these lines reflect a non-standard AGN ionising continuum, namely, a very hard spectrum lacking photons below a few KeV.

The analysis of the line profiles points out to a trend of increasing FWHM with increasing IP up to energies around 300 eV, where a maximum in the FWHM is reached. For higher IP lines, the FWHM remains nearly constant or decreases with increasing IP. We ascribe this effect to an increasing density environment as we approach to the innermost regions of these AGNs, where densities above the critical density of the CLs with IP larger than 300 eV are reached. This sets a strict range limit for the density in the boundary region between the narrow and the broad region of $10^8 - 10^9 \text{ cm}^{-3}$.

A relationship between the luminosity of the coronal lines and that of the soft and hard X-ray emission and the soft X-ray photon index is observed: the coronal emission becomes stronger with both increasing x-ray emission (soft and hard) and steeper X-ray photon index, i.e. softer X-ray spectra. Thus, photoionization appears as the dominant excitation mechanism. These trends hold when considering Type 1 sources only; they get weaker or vanish when including Type 2 sources, very likely because the X-ray emission measured in the later is not the intrinsic ionising continuum.

Subject headings: galaxies: active — infrared: galaxies — galaxies: Seyfert

1. Introduction

Coronal lines (CLs) are emission features arising from forbidden transitions of excited states of highly ionized species ($h\nu_{ion} \geq 100$ eV), implying the existence of very energetic processes occurring in or near the narrow line region (NLR). Torus (Pier & Voit 1995), close or in part of the broad line region (Shuder & Osterbrock 1981; Cohen 1983), NLR (Pelat, Alloin & Bica 1987; Appenzeller & Östreicher 1988) and extended narrow line region (ENLR) (Korista & Ferland 1989; Murayama, Taniguchi & Iwasawa 1998) have been proposed as possible locations for the formation of these lines in active galactic nuclei (AGNs).

CLs, also referred by some authors as Forbidden High Ionization Lines (FHILs), are

excited by collisions. What it is not clear is the type of mechanism responsible of the high ionization of the species. Two basic processes has been proposed in order to explain the high level of ionization: photoionization due to the central source, which emits an intense ionizing continuum, particularly hard UV and soft X-ray (Shields & Oke 1975; Grandi 1978; Penston et al. 1984; Korista & Ferland 1989; Ferguson et al. 1997; Oliva, Marconi & Moorwood 1999); and shocks between high velocity clouds and the narrow line region gas, i.e., collisional ionization much alike of the process occurring in the solar corona (Osterbrock & Parker 1964; Oke & Sargent 1968). There exists a third intermediate possibility: a combination of the above two processes (Viegas-Aldrovandi & Contini 1989). Recent works conclude that although nuclear photoionization is the main excitation mechanism, in order to reproduce adequately the observed emission line ratios, a contribution of shocks is necessary (Rodríguez-Ardila et al. 2006; Geballe et al. 2009).

Since the mid 70s, it has been claimed that optical CLs tend to be broader than lower ionization forbidden lines and its centroid position blueshifted with respect to the systemic velocity of the galaxy (Grandi 1978; Cooke et al. 1976; Penston et al. 1984). Indeed, a correlation is found between the ionization potential (IP) necessary to create the ionized specie and the line width (Wilson 1979; Pelat, Alloin & Fosbury 1981; Evans 1988). All together, this result is interpreted as the coronal region be located between the narrow and the broad line region and subjected to radial motions in some cases, probably associated to outflows (Penston et al. 1984; Ward & Morris 1984).

With the recent generation of high-sensitive detectors in the near infrared region (NIR), observations of a significant number of Seyfert galaxies has now been possible (Giannuzzo, Rieke & Rieke 1995; Prieto & Viegas 2000; Lutz et al. 2002; Rodríguez-Ardila et al. 2002; Reunanen, Kotilainen & Prieto 2003; Riffel, Rodríguez-Ardila & Pastoriza 2006; Geballe et al. 2009; Müeller Sánchez et al. 2011). As a consequence, new CLs have been added up to list (i.e., [S VIII], [S IX], [Fe XIII], [Si VI], [Si VII], [Si IX], [Si X], [Ca VIII]) allowing a revision of previous findings and a more consistent analysis of a complex emitting region. Among the most important results that can be mentioned are that the CLR is not restricted to the unresolved nucleus although it does not extended to the kpc range. Prieto et al. (2004); Rodríguez-Ardila et al. (2006), for instance, detect CLs at distances of up to a few hundreds of parsecs from the nucleus. These authors also report that the highest ionized species show the smallest emitting region size of the NLR, which is in agreement with photoionization from the nucleus. These results gathered additional support by the recent work of Müeller Sánchez et al. (2011), who studied the spatial distribution and kinematics of the NLR and CLR of seven AGN usign SINFONI and OSIRIS near-IR AO-assisted integral field spectroscopy at spatial scales ranging from 4 to 36 pc. They found that the two regions present a bright compact core and extended emission, with the CLR being more compact than the NLR, with typical sizes of the former between 80

and 150 pc in radius. Moreover, both regions display a similar dispersion velocity although the high-ionization gas presents more deviant behavior with velocity fields dominated by non-circular motions, associated to outflows.

The aims of this paper are twofold. First, to carry out the largest compilation of CLs published to date in the near infrared region (0.8-2.4 μm) and second, from the study of this database, to draw clues about the excitation mechanisms of these lines by looking for a connection between their luminosity and broad-band measurements in other spectral regions. As the sample contains a significant number of Type 1 (Ty1, hereafter) and Type 2 (Ty2, hereafter) AGNs, a discussion of viewing angle effects and thus the most likely location of the CLR will be done. This paper is structured as follows. Section 2 describes the selection of the sample; Section 3 presents the main results, with emphasis of the relation between FWHM and IP; the relation of CLs with soft and hard X-rays is discussed in section 4 and Section 5 contains the Summary and main conclusions.

2. Sample Selection

The sample of AGNs chosen for this work was selected primarily from the galaxies studied by Riffel, Rodríguez-Ardila & Pastoriza (2006, RRAP06). It includes 47 Seyferts and quasars observed in the wavelength interval 0.8-2.4 μm and collected using cross-dispersed spectroscopy at IRTF. Description of the conditions of the observations, instrumentation details and reduction process can be found in RRAP06.

RRAP06 sample was complemented with an additional sub-sample of active galaxies with published data on CLs covering a similar wavelength interval. These objects are: Circinus (Oliva et al. 1994; Müller Sánchez et al. 2006), NGC 1068 (Marconi et al. 1996; Thompson 1996; Rodríguez-Ardila et al. 2006), Mrk 335, Mrk 1044, Ton S180, NGC 863 (Rodríguez-Ardila et al. 2002), Mrk 766 (Rodríguez-Ardila, Contini & Viegas 2005), Mrk 1210 (Mazzalay & Rodríguez-Ardila 2007) and Mrk 78 (Ramos-Almeida et al. 2006). Basic information of the selected galaxies is shown in Table 1. The objects are listed in increasing order of right ascension. The final sample is composed of 54 AGNs: 36 of Ty1 (19 of which are narrow line Seyfert 1, NLS1) and 18 of Ty2. Values of redshifts were taken from the NED database. The last column indicates whether or not the galaxy displays at least one CL (at 3σ detection) in the 0.8–2.4 μm region. Objects marked with “N” do not show CLs in the the NIR spectrum. Yet, some of the them have CLs in other spectral ranges: these are: Mrk 334 ([Fe x] $\lambda 6374$, Osterbrock & Martel (1993) and [Ne v] $14.3\mu\text{m}$, Prieto & Viegas (2000)), NGC 1144 ([Ne v] $14.3\mu\text{m}$, Prieto & Viegas (2000)), NGC 2110 ([Fe VII] $\lambda\lambda 5721, 6087$ and [Fe x] $\lambda 6374$, Shuder (1980)), NGC 5929 ([Fe x] $\lambda 6374$, Osterbrock & Martel (1993)) and

Mrk 493 ([Fe VII] $\lambda 6087$, Crenshaw et al. (1991)). All other AGN marked with “N”, to our knowledge, do not display any coronal lines either in the NIR or in any other wavelength region.

3. Results

3.1. Frequency of coronal lines

The CLs that fall in the spectral window 0.8–2.4 μm are [S VIII] 0.9913 μm , [Fe XIII] 1.0747 μm , [S IX] 1.252 μm , [Si X] 1.4301 μm , [S XI] 1.9196 μm , [Si VI] 1.9630 μm , [Al IX] 2.0450 μm and [Ca VIII] 2.3213 μm (See Tab 3). Few objects in the sample display all them simultaneously. For each object with at least one CL detected, Figures 1 to 7 show a zoom of the spectral region containing the CL. We found that 36 out of 54 galaxies (66%) display at least one CL. Of the remaining 18 sources, five of them show CLs in other spectral ranges (optical and/or mid-IR), as reported in the literature (see Sect. 2). Adding these 5 objects, the number of AGN with at least one CL - i.e. from ions with IP ≥ 100 eV - in any range of the spectrum increases to 41, that is, 76% of the sample.

Table 2 lists the CLs fluxes measured in sample along with fluxes of the narrow components of Pa α and Br γ , except when indicated. Because of discrepancies either in the line fluxes or in the uncertainties relative to the values published by RRAP06 in some cases, we have reviewed all their measurements and these are the ones presented in Table 2. In cases of line blending, a multiple Gaussian fit was applied. Upper limits are reported for the expected position of the lines if they were not detected above 3σ level.

It is easy to see from Table 2 that for all $3\text{-}\sigma$ detections, the most frequent and conspicuous CLs in the sample are those of silicon and sulfur, and among those, the ones with the lowest IP (< 300 eV) are the strongest. CLs from other elements, e.g., Ca, Al or Fe, are less frequent and weaker, the former two being affected by metallicity effects and depletion onto dust, while the later may be not be that much affected. Indeed, the iron optical coronal lines are rather strong. [Fe VII] 6087 \AA for instance, is even stronger than the strongest NIR CL [Si VI] 1.963 μm (e.g. Rodríguez-Ardila et al. (2006)). Yet, the [Fe XIII] 1.0747 μm line traced in this work is located in wing of the strongest NIR line, He I 1.0830 μm , which most probably hampers its detection in most cases. Overall, [Si VI] 1.963 μm , [S VIII] 0.991 μm , [Si X] 1.431 μm and [S IX] 1.252 μm are the lines with the largest number of detections, being observed in 30, 24, 22 and 20 objects, respectively. For that reason, the rest of the analysis shall focus on these lines only.

Figure 8 shows a histogram with the number of galaxies per bin in luminosity (full

line for Ty1 and dashed line for Ty2) in each of the above four lines. Upper limits are not included. Broadly speaking, the distribution in luminosity for both types of AGNs is similar, with most lines located in the interval $\log L$ 39-40 ergs^{-1} and the whole sample spanning 3 dex in full-width around that interval. Note that the numbers above are similar to the range of $[\text{Fe x}]$ 6374 Å luminosity reported by Gelbord et al. (2009) using a sample of 63 AGN with strong high-ionization emission lines, none of them common to our sample. Figure 8 also suggests a similar percentage between the two types of AGNs that display $[\text{Si x}]$ and $[\text{S ix}]$ ($\sim 40\%$ and $\sim 35\%$, respectively). Ty2, however, slightly outnumber Ty1s in the lower ionization CLs $[\text{Si vi}]$ and $[\text{S viii}]$: 67% vs 50% and 56% vs 39%, respectively. These differences can be attributed to the relatively higher redshift - z - of Ty1 objects, making the detection of CLs more difficult due to the poorer spatial resolution sampling. In addition, when $z > 0.035$, both lines start falling in low atmospheric transmission zones or strong telluric absorption, hindering their detection. Note that only one Ty2 of the sample (Mrk 78) has $z > 0.03$ while $\sim 35\%$ of Ty1s exceeds this redshift.

Similar results on the frequency of coronal line emission in Seyfert galaxies regardless of their type have been reported in the literature, albeit on the basis of smaller samples. Most of these works are conducted in the NIR (e.g Prieto & Viegas 2000; Reunanen, Kotilainen & Prieto 2003; Rodríguez-Ardila et al. 2006; Prieto, Marco & Gallimore 2005) and mid-IR (e.g. Prieto & Viegas 2000). They all sample CLs from elements including Si and Mg, which could get easily depleted from the gas phase if dust is present. Yet, all these works show that Ty2 objects show as rich and strong CL spectra as those of Ty1. However, analysis done on the basis of the optical CL spectrum, mainly on iron lines, indicate opposite results. Works done by Murayama & Taniguchi (1998); Nagao, Taniguchi & Murayama (2000) and Gelbord et al. (2009), for instance, remark a significant weaker optical CL in Ty2 than in Ty1s. These authors argue that the frequency and strength of the CL spectrum should thus depend on the orientation of the torus with the line of sight, being in Ty2 sources partially or totally obscured. As a consequence, the CLR should form at the inner face of the torus.

Two relevant issues may explain these conflicting results. First, the extinction in the NIR is a factor 10 lower than in the optical. As Ty2 sources are more absorbed, this has a definitive impact on the detection and the measurement of optical CLs, mostly considering that they are relatively weak features. Indeed, a recent discovery of a Ty2 quasar with an outstanding high-ionization spectrum and zero internal extinction (Rose et al. 2011) supports this argument. In moving to the NIR, the situation changes dramatically for strongly reddened sources. Prototype Ty2 AGNs such as NGC 1068 or Circinus, not only show the full spectrum of CLs (i.e., Si, Al, Ca, among others), but in addition, these are the dominant lines in their spectra (Moorwood et al. 1996; Reunanen, Kotilainen & Prieto 2003; Müller Sánchez et al. 2009, 2011).

Second, spatial resolution should be taken into account in Ty2s for CL detection, especially in the optical but also in the NIR. Circumnuclear star formation, which is often more relevant in Ty2s, increases the continuum level with the corresponding loss of line contrast. A striking illustration of this effect is the nucleus of Centaurus A. It shows no CLs either in optical or in the NIR in seeing limited conditions (Reunanen, Kotilainen & Prieto 2003). But observations with adaptive optics reveal the K-band CLs of [Si VI] $1.963 \mu\text{m}$ and [Ca VIII] $2.34 \mu\text{m}$ (Neumayer et al. 2007).

Additional arguments against the CLR being obscured by the torus can be gathered from Circinus, NGC 1068 and Centaurus A. They all are extreme Compton thick sources even in the hard X-rays. Under that condition, it is difficult that any optical CL emission could be seen if their bulk is produced in the inner face of the torus. Moreover, the high spatial resolution studies conducted by Rodríguez-Ardila et al. (2006) and Mazzalay, Rodríguez-Ardila & Komossa (2010) show that Ty2 sources display strong [Fe VII], [Fe X] and [Fe XI] lines, with emitting regions extending to distances of a few hundred parsecs from the centre in the case of NGC 1068. That is, well beyond the expected size of the putative torus. Moreover, a dusty CLR implies a very weak coronal line spectrum because of the absorption of the incident continuum by dust at large U(H) Ferguson et al. (1997). Although we do not rule this later hypothesis for those objects where no coronal lines are seen, at least those that display CLs should have the bulk of the CLR outside the torus.

In spite of the difference in coronal line luminosity between the galaxies, covering 3 dex in each of the four lines considered (see Fig. 8), the flux ratios [Si VI]/[Si X] and [S VIII]/[S IX] are distributed in a very narrow interval of values, as can be seen in Fig 9. Moreover, no distinction between Ty1 and Ty2 AGNs is observed in both ratios, giving additional support to our previous finding of similar frequency of CLs in both type of objects. Note that these two ratios are independent of the metallicity as they contain ions of the same element. The abscissa is strongly sensitive to the form of the ionizing continuum because the difference in IP between [Si VI] and [Si X] is 184 eV (see Table 3) while the ordinate ([S VIII]/[S IX]) is not: the difference in IP between both ions is only ~ 50 eV. It is easy to see that the scatter in the former ratio is restricted to 0.7 dex, with an average value of the ratio equal to 1.4. For the later, it is no larger than 0.4 dex, with an average of 1.1. Clearly, the bulk of CL fluxes should be produced outside the torus region because the two ratios and their scatter are very similar in Ty1 and Ty2 AGNs. Observational evidence of this scenario was recently obtained by Müller Sánchez et al. (2011). They quantified the extent of the CLR by means of azimuthal averages within circular radial annuli of the flux distribution of [Si VI] in a sample of seven AGNs, four of them common to our sample (Circinus, NGC 1068, NGC 4151 and NGC 7469). Their results show that the flux distribution is resolved and extended, supporting an origin of the CLs in the inner part of the NLR or in the transition region between the BLR and

the NLR.

Recent studies (Whittle et al. 2005; Schlesinger et al. 2009; Mazzalay, Rodríguez-Ardila & Komossa 2010) have pointed out photoionization as the main driver for the coronal lines. Yet, we note that detailed analysis of CL flux ratios as done in Rodríguez-Ardila et al. (2006) on the basis of $[\text{Fe X}]/[\text{Fe VII}]$ vs $[\text{Fe XI}]/[\text{Fe VII}]$ or $[\text{Fe XI}]/[\text{Fe X}]$ show that photoionization alone is not enough. Photoionization models predict the general trend of these ratios but specific values are not matched even if considering new calculations of collision strengths for iron. Rodríguez-Ardila et al. (2006) show that adding the extra power of shocks of different velocities to photoionization improves the match between the observed iron ratios and those predicted. Note that AO observations of the CLR carried out by Müeller Sánchez et al. (2011) support this picture. They found kinematic signatures of outflows in NIR high-ionization lines of a sample of nearby AGNs, with the radio jet clearly interacting with the ISM, indicative of a link between jet power and outflow power.

The lack of coronal lines above certain energies may be related to a deficient ionizing continuum. This would explain why some objects display $[\text{Si VI}]$ (IP=166 eV) and $[\text{S VIII}]$ (IP=280 eV) but not lines of higher IP. Examples of this among the nearest objects in the sample are Mrk 1066, NGC 5728 - both lacking lines with IP > 166 eV or NGC 3227 and NGC 7682 - both lacking lines of IP > 280eV (see Table 2). A similar argument applies to some of the objects studied by Mazzalay, Rodríguez-Ardila & Komossa (2010) on HST/STIS spectra: some of their objects, including NGC 3227, display $[\text{Ne V}]$ and $[\text{Fe VII}]$, both with IP ~ 100 eV, but not higher optical ionization lines. The results for NGC 3227 are further supported by Rodríguez-Ardila et al. (2006), who report on the non detection of $[\text{Fe XI}]$ 7892Å (IP=260 eV).

Distance should also play a major role in the detection of CLs: these are relatively weak features and loose of contrast over the stellar continuum light in low-luminosity nearby AGNs hampers their detection. This argument is supported by results derived from Riffel et al. (2009), who modeled the NIR continuum emission of AGNs in terms of stellar population, AGN featureless continuum and hot dust in 9 Ty1 and 15 Ty2 galaxies. These 24 sources are also studied in this work using the same set of data. Cross-crossing Riffel et al.’s results with ours allow us to conclude that for most Ty1 and Ty2 objects where no CLs are detected, the contribution of the stellar population dominates the observed NIR continuum (see Table 3 of Riffel et al. 2009). For example, in the Ty1 sources NGC 1097 and Arp 102 B, 96% and 89%, respectively, of the observed continuum is due to stars. Similarly, in the Ty2s NGC 1144, NGC 5929 and NGC 5953, more than 90% of the observed continuum is due to that component.

In high-luminosity AGNs, the strong continuum emitted by the central source would also

dilute the CLs, in a similar way the stellar population affects the CLs in nearby sources. Note that the effect of dilution, in this case, gets severe with increasing z . Observational evidence of this hypothesis can be gathered by examining the work of Glikman, Helfand & White (2006), who constructed the first quasar composite spectrum in the NIR using a sample of 27 quasars with z between 0.118 - 0.418. A close examination to Glikman et al.'s data shows that no coronal lines are observed either in the individual sources nor in the composite template. Indeed, the only forbidden line that is clearly detected is [S III] 0.906 μm . Under the assumption that photoionization by the central engine is the dominant source of gas excitation, dilution by the AGN continuum would preferentially affect lines emitted by the NLR. Thus, the line flux ratio $\text{Pa}\alpha/[\text{S III}]$ 0.906 μm can be used as a metric for this effect. Note that the total flux (narrow + broad) of $\text{Pa}\alpha$ can be employed here as the broad component of that line dominates the line flux in Ty1 sources.

The value of the above ratio measured in the composite NIR quasar spectrum of Glikman, Helfand & White (2006) is 12.4 (See Table 6 of that work). Dilution would tend to increase that value. In our sample, nearby Ty1 sources have ratios approaching 4 at most (1H 1934-063, NGC 4748 for instance) while PG 1612+261 ($z=0.1309$) has a ratio of 11.6. In very luminous objects like Mrk509 ($z=0.034$), that ratio reaches to 30. These results evidence that the AGN continuum indeed dilutes the features emitted by the NLR in luminous sources. Note that [S III] 0.906 μm is the strongest forbidden line observed in the NIR, being at least $5\times$ stronger than [Si VI] 1.963 μm , the strongest coronal line of our survey.

The z range of our sample is $0.0015 < z < 0.5$, median ~ 0.02 , $1'' \sim 420$ pc (Table 1), and in general, most objects with $z < 0.005$, $1'' < 110$ pc, show CLs, although not always in the full range of ionization potentials. Above this z , there are a size able number of objects with coronal emission, some with a remarkable spectrum, e.g. Mrk 573 (Ty2), $1'' \sim 360$ pc, whereas others at equivalent or inferior distances do not show emission despite of the high Signal-to-Noise ratio (S/N) of the spectra, eg. NGC 1275 (Ty2) or NGC 1144 (Ty2), both at similar distance as Mrk 573 (Table 2).

All the above suggest that aside physical parameters (ionizing continuum, metalicity, gas density or dust) observational issues like S/N or the spatial scale in the sky, strongly influence the detection of coronal lines. In the following sections we will collect information from the NIR to increase our knowledge of the physics of the CLs to complement the picture already gathered from the visible region.

3.2. Kinematics of the coronal line region

This section explores the correlation between the ionised gas velocity, as measured by the line FWHM, and the ionization level of the gas, as measured by the IP of the corresponding line. If photoionization is the major mechanism, a correlation between these two parameters is expected. This is because the highest the gas ionization level (high IP), the closer to the nucleus is its location, therefore, the greatest is its motion within the gravitational potential wells of the super massive black hole and host galaxy. Coronal lines are very suitable to study this prediction given the high range of IPs they cover. Most of the results published to date have been drawn from the study of small number of objects and CLs. The larger number of galaxies examined here and the inclusion of eight CLs of different ions and wide range of IP allow us to investigate the FWHM-IP relationship in more detail.

In the late 70s, Wilson (1979) reported for NGC 3783 a strong correlation between FWHM and ionization potential of various optical forbidden lines, with the CLs showing the largest FWHM and low or medium ionization lines the smallest ones. Later works reported a similar trend in other active galaxies with either optical or NIR lines (Osterbrock 1981; Pelat, Alloin & Fosbury 1981; Penston et al. 1984; Thompson 1995). Conversely, Giannuzzo, Rieke & Rieke (1995) found that CLs show an ample variety of FWHMs, leading to the conclusion that the CLR occupies different regions in different galaxies. Reunanen, Kotilainen & Prieto (2002, 2003) study the CLs in the 1.5-2.5 μm range in 14 Seyfert galaxies. In only four of them a positive correlation between FWHM and IP could be established. Rodríguez-Ardila et al. (2002) in a sample of six galaxies (5 classified as NLS1), found a positive correlation in three of them. Other observations have also shown that CLs can display no correlation at all or even an anti-correlation between FWHM and IP. Such is the case of NGC 4151 (Knop et al. 1996), where [S XI] 1.9196 μm has a FWHM significantly lower than the narrow component of Pa β . Similarly, Marconi et al. (1996) reported for NGC 1068 FWHM values for [Fe XI] 0.7892 μm and [Si IX] 3.9350 μm smaller than those of [Fe II] 1.257 μm whereas Rodríguez-Ardila et al. (2006) and this work (Table 4) find the opposite: low- and intermediate- ionization lines present FWHMs smaller or at least comparable to those of the optical and near-IR CLs.

Table 4 lists the FWHM of the CLs (corrected from instrumental width, 360 km s⁻¹) along with the FWHM of [S III] 0.953 μm and [Fe II] 1.257 μm , two of the strongest medium- to low-ionization lines detected in the galaxy sample. In order to measure the FWHM the emission lines were assumed to be well represented by a single or a combination of Gaussians profiles (see Figs. 1 to 7). The LINER routine (Pogge & Owen 1993) was used in this process.

Figures 10 and 11 show plots of FWHM vs IP for each of the galaxies in the sample

that display at least two coronal lines. For comparison purposes, the FWHM of the lower ionization lines [S III] $0.953\mu\text{m}$ and [Fe II] $1.257\mu\text{m}$ are also included. It can be seen that in some of the AGNs with sufficient number of CLs, a trend of increasing FWHM with IP is observed but up to energies of about 200–300 eV. In following this trend, we focus on the strongest CLs, namely those from Si and S, and ignore those of Fe and Ca as they are overall weaker and their FWHM more difficult to measure or subjected to larger uncertainties. At higher energies the FWHM, in particular of the most conspicuous and frequent lines, namely [S IX] and [Si X], remains constant or start decreasing with increasing IP. These are, for example, the cases of Mrk 335, ESO 428-G14, Mrk 1210, Mrk 1239, NGC 4051, Mrk 766, Ark 564, NGC 7469, NGC 7674 and tentatively, Circinus. We have labeled these objects as “P” (peak at about 300 eV) in the last column of Table 4. In contrast, NGC 4151 and NGC 5548, two of the galaxies with the highest S/N in the sample, the FWHM shows no dependence with IP. In both objects, some CLs have widths comparable or even smaller than those displayed by low-ionization lines, confirming previous results reported by Knop et al. (1996). All other remaining objects do not show a trend or it is difficult to evaluate it because all emission lines are unresolved.

Table 4 and Figures 10 and 11 allow us to state that overall, no particular trend between FWHM and IP is seen in regard to the type of AGN. The subset of galaxies that we have labeled “P” contains similar proportion of both types of objects. Similarly, for the objects where no trend is seen, no difference between Ty1 and Ty2 is observed, reinforcing the results already discussed in the preceding section. That is, a CLR located outside the torus region. Differences observed from object to object is rather due to variations in the physical properties rather than to a viewing angle dependence.

The increase of FWHM with IP up to a peak energy of about 300 eV is interpreted as due to a combined effect of increasing electron density gradient towards the centre and spatial extension of the CL gas. The critical density of [S VIII] (IP=280.9 eV) and that of [S IX] (IP=328.2 eV), two of the most common lines in the sample, are the highest among the CLs studied: $n_e = 4 \times 10^{10}$ and $2.5 \times 10^9 \text{ cm}^{-3}$, respectively. Thus, their critical density sets up an upper limit for the n_e in the coronal line region to be $< 10^9 \text{ cm}^{-3}$. However, the CLs with higher IP (i.e., [Si X], [S XI] and [Fe XIII]) have critical densities lower than the above values, by almost an order of magnitude (see Table 3). Therefore, if the density increases steeply towards the center to values $\geq 10^8 \text{ cm}^{-3}$, these later two high IP lines might get severely suppressed. Specifically, their high-velocity component would not be observed due to collisional de-excitation. Only their low velocity component - which should arise further out from the center - would be seen. This would explain the observed decrease or constancy of the line FWHM with IP.

It is difficult to ascribe the absence of high velocity component in high IP lines to dust: absorption of the ionising photons will affect low and high velocity gas components alike. Depletion of the gas phase on dust is also not realistic as that will tend, if any, to reduce the low velocity component of the gas, which is formed further out from the dust sublimation radii, instead of the high velocity one (see Ferguson et al. 1997). In this respect, silicon lines, which should be largely depleted, show [Si X] $1.43 \mu\text{m}$ (IP=351 eV) with FWHM comparable to that of [Si VI] $1.963 \mu\text{m}$ (IP =167 eV) but still smaller than that measured for [S VIII] (IP=280) which is little affected by depletion. Clear examples are NGC 262, MCG 05-13-17, ESO 428-G014, Mrk 1210, NGC 4151, Mrk 766, NGC 5548 and NGC 7469.

The results above allow us to conclude that (i) a strict limit for the density in the interface region between the coronal and the broad line region can be set in the range $10^8 < n_e < 10^9 \text{ cm}^{-3}$; (ii) the expected FWHM-IP correlation is modulated by the critical density of the corresponding ion. If a wide range of densities is present in the NLR - CLR region, we may indeed expect a strong correlation between the FWHM and the critical density, as already put forward by Pelat, Alloin & Fosbury (1981); Penston et al. (1984); De Robertis & Osterbrock (1986) and Ferguson et al. (1997).

4. The relation between the coronal and X-ray emissions

In order to produce the observed CLs, ionizing energies in the range 127–450 eV are necessary. If photoionization by a central source is the dominant excitation mechanism, a positive relation between X-ray strength and the coronal line luminosity is expected. Attempts have been made in order to look for connections between X-rays and CLs intensities but with conflicting results. Penston et al. (1984) found no correlation between [Fe X] $\lambda 6374$ and the X-ray 2–10 keV luminosity, $L_{2-10\text{keV}}$. Porquet et al. (1999) found, based on numerous data extracted from literature, a clear correlation between the luminosity of [Fe X] $\lambda 6374$ and the ROSAT X-ray luminosity, $L_{0.1-2.4\text{keV}}$. Similarly, a positive trend, both in flux and luminosity, between the CLs [O IV] $25.9 \mu\text{m}$ and [Ne V] $14.3 \mu\text{m}$ and the ROSAT $L_{0.1-2.4\text{keV}}$ emission is found by Prieto, Pérez García & Rodríguez Espinosa (2002). However, these authors found no correlation when considering the hard X-ray 2–10 keV luminosity.

Considering the large dataset gathered in this work, the possible relationship between the soft and/or the hard X-ray and the CL emission is explored in more detail. We choose [Si VI] $1.963 \mu\text{m}$ and [S VIII] $0.991 \mu\text{m}$ as representative lines of the coronal region as they are the most frequent in the sample. Moreover, this comparison allows us to see if there are differences between coronal lines emitted by refractory and non-refractory elements.

Figures 12 and 13 display the soft X-ray luminosity, L_x [soft], integrated either over the 0.1–2.4 keV or the 0.5–2.0 KeV interval, corrected by absorption, versus the luminosity of [Si VI] 1.963 μm , and [S VIII] 0.991 μm , respectively. Only Ty1 sources are included. The nature of the soft X-rays in Ty2 sources is questionable, in particular, in view of Chandra and XMM spectra, which show the X-ray emission resolved in emission lines (e.g. Bianchi, Guainazzi & Chiaberge 2006). Under low level activity, a few Ty1 sources have also shown a soft X-ray emission line spectrum (e.g. Nucita et al. 2010, and references therein). Still, the bulk of their emission is expected to be dominated by the AGN continuum light.

It can be seen from Figs. 12 and 13 a trend of increasing CL – with soft X-ray – luminosity. The linear correlation coefficient is 0.8 and 0.77, respectively, determined using all points, with no distinction between normal and NLS1 galaxies. The soft X-ray spans four orders of magnitude whereas the coronal luminosity just two, so the distance factor that stretch both axis should not be the major driver of the trend. These results are consistent with the trend found by Gelbord et al. (2009) using the luminosity of [Fe X] 6374 \AA line and that of the 0.1-2.4 keV band L_x .

Figures 14 and 15 show the power law photon index, Γ , of the soft X-rays as defined by Walter & Fink (1993) versus the coronal line luminosity for the same two lines. The linear correlation indices in these cases is lower: 0.31 and 0.62, respectively, very likely due to the scatter introduced by NLS1 galaxies, which are usually characterized by a prominent soft excess. Indeed, note that they have the largest values of Γ and a higher CL luminosity.

To our knowledge, only Erkens, Appenzeller & Wagner (1997) have explored the incidence of Γ on the CLs. They found that the values for the photon index are related to the equivalent width of [Fe X] 0.6375 μm , concluding that strong CL emission is present predominantly in AGNs with a soft excess ($\Gamma \geq 2.5$). Figures 14 and 15 also suggest a photon index threshold: most objects have Γ above 2. NGC 3227 has a harder spectrum (see both figures), meaning that it has a deficiency in high energy EUV photons when compared to sources with Γ above 2. It is interesting to note that its CL spectrum has also a clear threshold in IPs, as CLs with IP > 166 eV are barely detected (see Fig. 3 and Sect 3).

Regarding the hard X-rays, Figure 16 shows the absorption-corrected luminosity, $L_{2-10 \text{ keV}}$, versus the luminosity in [Si VI] 1.963 μm . For illustrative purposes, Ty2 sources are now included in the figure. There is a large scatter in the plot but it may be noticed that this is introduced by the Ty2 sources mostly, normal Ty1s and NLS1s follow a narrower trend, with a linear correlation index of 0.97. The number of objects with available hard X-emission is smaller, hence the reduced number of points in the figure as compared with those in Fig. 12 or 13. The same behavior is revealed when comparing with the [S VIII] luminosity - not shown. The positive trends found reinforce the scenario of photoionization by the central

source as the main mechanism for the formation of the coronal lines. The diagnosis fails however for Ty2 sources because of their heavy absorption, even in the hard x-rays –some are Compton thick, e.g NGC 1068, Circinus – so that their measured X-ray luminosity is not accounting for the true intrinsic value.

The results above firmly support a relationship between soft and hard X-rays and NIR coronal lines, explored for the first time in the literature here. They agree with previous findings obtained in other wavelength intervals (optical and mid-IR) claiming a correlation between the luminosity of the CLs and the X-ray emissions (soft and hard) (Porquet et al. 1999; Prieto, Pérez García & Rodríguez Espinosa 2002; Gelbord et al. 2009). We should keep in mind that the X-ray and NIR observations are not contemporaneous but that should not affect the outcome. This is because, on average, the largest uncertainty comes from the model dependence inherent in converting X-ray count rates to fluxes rather than to variability itself Gelbord et al. (2009).

On the other hand, to be an X-ray AGN emitter is not condition to be also a CL emitter. Indeed, all the sources in the sample are X-ray emitters. As discussed in Sect. 3, insufficient spatial resolution, specially for the more distant sources, hampers the detection of CLs. However, that is not always the reason. A clear counter example is NGC 1097, one of the nearest AGN in the sample, with $L(0.1- 2 \text{ keV}) = 5.0 \times 10^{40} \text{ erg s}^{-1}$ (Terashima et al. 2002) and no CLs so far detected (Table 2), even at distances from the centre of 10 pc (Muller-Sánchez et al. 2010, submitted). There are also AGNs with a truncated CL spectrum at lines with IP above certain energy. Examples include NGC 3227, with barely detected CLs with IP > 166 eV in the optical and IR (Rodríguez-Ardila et al. 2006, this work, see sect.3); Mrk 3, with no CLs with IP > 100 eV within 10 pc from the centre (Mazzalay, Rodríguez-Ardila & Komossa 2010). Some possibilities for the CL absence may include a particular type of ionizing continuum, i.e., one that is intrinsically different from that of an standard AGN, or is modified by intervening material located in between the central source and the CL region. Such material could be the the warm absorber seen in some Seyfert galaxies (Nandra & Pounds 1994; Reynolds 1997), which could significantly modify the form of the input ionizing continuum. Porquet et al. (1999) proposed that this structure can also be a source of coronal lines.

Another possibility is that the ionised gas in Ty2 galaxies have different distributions in different sources (Sambruna et al. 2001a,b). This hypothesis was raised in the light of *Chandra* observations of Mrk 3 and Circinus. While in the former most of the line emission in X-rays is spread over several hundred parsecs, this is not the case in the latter, where the ionized gas is highly concentrated, with most of the flux originating within the central 15 pc.

5. Summary

The first study aimed at studying the physical properties of near-IR CLs spanning the energy range 130 – 450 eV are derived for the first time on a sizable sample of AGNs (54 sources). The main results are as follows.

CLs in the 0.8–2.4 μm interval with IP >127 eV are detected in 2/3 (36 AGNs) of the galaxy sample. CLs are formed very close to the central source. Due to lost of line contrast in an increasing continuum level, their detection depends largely on source distance. However, we confirm the existence of nearby objects, e.g. NGC 1097, NGC 5963, where the absence of CLs is genuine. These objects must have a suppressed ionising continuum lacking photons with energies ≥ 100 eV.

Among the CLs and species studied in this work, from S, Si, Fe, Ca and Al, those coming from the the most abundant elements are the most frequent, namely Si and S. And among these, those from the lowest IP, i.e [Si VI] 1.963 μm (IP=166 eV) and [S VIII] 0.991 μm (IP=280 eV) are the most common ones. On the basis of these two lines, Ty2 sources with CLs outnumber Ty1 by $\sim 17\%$. However, this discrepancy is attributed to differences in z : Ty1 sources have significantly larger z than Ty2 and the two lines fall in regions of poor atmospheric transmission when $z > 0.035$. Focusing on the highest ionization lines, which are believed to be formed at the innermost regions of the AGN, their presence in both types of AGNs in similar proportions (Fig. 8) implies that their spatial location has to be outside the inner face of the torus. Thus, orientation effects do not play a role in the detection of coronal lines.

The luminosity of the coronal emission is distributed in a narrow interval, covering 3 dex at most. Moreover, the luminosity distribution of the four most frequent coronal lines studied ([Si VI], [S VIII], [Si X] and [S IX]) is strongly peaked, with the largest number of objects located between $\text{Log } L \sim 39$ and ~ 40 $\text{erg s}^{-1} \text{cm}^2$. [Si VI] 1.963 μm is the most luminous of the coronal lines analyzed, confirming previous studies that use it as an indicator of nuclear activity.

A strong prediction of photoionization models, assuming a simple relation between the cloud distance and its velocity, is a correlation between the line FWHM and the IP of the corresponding ion. We see a trend of increasing FWHM with IP but up to energies of about 300 eV (Table 4). Above this peak energy, the FWHM remains constant or decreases with IP. We ascribe this effect to a combination of increasing electron density towards the center and the spatial extension of the coronal gas. In a photoionized gas, the highest the IP the closer to the center a line is produced. Coronal lines with the highest IP have critical densities approaching 10^8 cm^{-3} . If the density in the innermost region of the NLR is significantly higher

than that, those lines will be severely affected by collisional de-excitation and their high-velocity component will get suppressed. Accordingly, only their lower velocity component, which might come from a further region from the center, would be seen. This would explain why the FWHM of [S VIII] is the highest for most sources: it is the coronal line with the highest critical density. Its intensity is not affected by collisional de-excitation as the lines of higher IP likely are. This scenario sets a strict limit for the density in the boundary region between the narrow and the broad regions of $10^8 - 10^9 \text{ cm}^{-3}$.

Further support to photoionization as the main mechanism to excite the CLs arises from the positive trends found between the X-ray luminosity –soft and hard, the soft power-law photon index and the coronal line luminosity. In particular, objects with the softest X-ray spectrum tend to have strong CLs, this being expected considering that the CLs surveyed in this work require energies in the 0.1 - 0.5 keV interval. These trends hold when considering Ty1 sources only; they get weaker or vanish when including Ty2 sources. We believe this is because the X-ray emission measured in these cases is not representative of the intrinsic AGN power. Some of the Ty2 sources are, indeed, Compton thick so even their 2-10 Kev spectrum may just be reprocessed emission. Other sources, like circumnuclear star formation, line emission and bremsstrahlung are dominating the emission even in the hard X-rays.

The presence of truncated CL spectra in some objects, i.e., lacking CLs above a certain IP, could be ascribed to a specific geometrical configuration, where the line of sight between the NLR gas and the soft X-ray continuum is blocked by material that absorbs photons above a certain energy (a warm absorber, for example). It may also be possible that centrally illuminated ionized gas in Seyfert galaxies can have very different distributions in different sources. Alternatively, these objects may have an special type of ionizing spectrum, lacking ionizing photons above a certain energy threshold. However, neither the corresponding X-ray spectral index nor the X-ray luminosity differentiate objects with and without CLs because they both share similar values in these two properties.

This research has been supported by the Instituto Colombiano para el Desarrollo de la Ciencia y la Tecnología, Francisco José de Caldas, (Colciencias), code 1101-05-17607, contract RC 206-2005 and by the Brazilian agency CNPq (308877/2009-8) to ARA. We are grateful to an anonymous Referee for a careful and critical reading of the manuscript.

REFERENCES

Alexander D. M., Young S., Hough J. H. 1999, MNRAS, 304, L1

- Appenzeller I., Östreicher R. 1988, *AJ*, 95, 45
- Bassani L., Dadina M., Maiolino R., Salvati M., Risaliti G., Della Ceca R., Matt G., Zamorani G. 1999, *ApJS*, 121, 473
- Bianchi, S., Guainazzi, M., Chiaberge, M. 2006, *A&A*, 448, 499
- Cappi M. et al. 2006, *A&A*, 446, 459
- Cohen R. D. 1983, *ApJ*, 273, 489
- Cooke B. A., Elvis M., Maccacaro, T., Ward M. F., Fosbury A. E., Penston M. V. 1976, *MNRAS*, 177, 121P
- Crenshaw D. M., Peterson B. M., Korista K. T., Wagner R. M., Aufdenberg, J. P. 1991, *AJ*, 101, 1202
- De Robertis, M. M., Osterbrock, D. E. 1986. *ApJ*, 301, 727
- Erkens U., Appenzeller I., Wagner S. 1997, *A&A*, 323, 707
- Evans I. N. 1988, *ApJS*, 67, 373
- Ferguson, J. W., Korista, K. T., Ferland, G. J. 1997, *ApJS*, 110, 287
- Ferland G. J. 1993, Department of Physics and Astronomy Internal Report, University of Kentucky
- Geballe, T., Mason, R., Rodríguez-Ardila, A., Axon, D. 2010, *ApJ*, 701, 1710
- Gelbord, J. M., Mullaney, J. R., Ward, M. J. 2009, *MNRAS*, 397, 172
- Giannuzzo E., Rieke G. H., Rieke M. J. 1995, *ApJ*, 446, L5
- Glikman, E., Helfand, D. J., White, R. L. 2006, *ApJ*, 640, 579
- Grandi S. A. 1978, *ApJ*, 221, 501
- Guainazzi M., Matt G., Perola G. C. 2005, *A&A*, 444, 119
- Kaspi S., Maoz D., Netzer H., Peterson B., Vestergaard M., Jannuzi B. T. 2005, *ApJ*, 629, 61
- Knop R. A., Armus L., Larkin J. E., Matthews D. L., Shupe D. L., Soifer B. T. 1996, *AJ*, 112, 81

- Korista K. T., Ferland G. J. 1989, *ApJ*, 343, 678
- Leighly K. M. 1999, *ApJS*, 125, 317
- Levenson N. A., Weaver K. A., Heckman T. M. 2001, *ApJ*, 550, 230
- Lutz D., Maiolino R., Moorwood A. F. M., Netzer H., Wagner S. J., Sturm E., Genzel R. 2002, *A&A*, 396, 439
- Maiolino R., Krabbe A., Thatte N., Genzel R. 1998, *ApJ*, 493, 650
- Marconi A., van der Werf P. P., Moorwood A. F. M., Oliva E. 1996, *A&A*, 315, 335
- Mazzalay X., & Rodríguez-Ardila A. 2007, *A&A*, 463, 445
- Mazzalay X., Rodríguez-Ardila A., Komossa, S. 2010, *MNRAS*, 405, 1315
- Moorwood A. F. M., Lutz D., Oliva E., Marconi A., Netzer H., Genzel R., Sturm E., de Graauw Th. 1996, *A&A*, 315, L109
- Müller-Sánchez F., Davies R. I., Eisenhauer F., Tacconi L. J., Genzel R., Sternberg A. 2006, *A&A*, 454, 481
- Müller-Sánchez, F., Davies, R. I., Genzel, R., Tacconi, L. J., Eisenhauer, F., Hicks, E. K. S., Friedrich, S., Sternberg, A. 2009, *ApJ*, 696, 448
- Müller-Sánchez, F., Prieto, A., Hicks, E. K. S., Vives-Arias, H., Davies, R. I., Malkan, M., Tacconi, L. J., Genzel, R. 2011, Accepted in *ApJ*, arXiv:1107.3140.
- Murayama T., Taniguchi Y. 1998, *ApJ*, 497, L9
- Murayama T., Taniguchi Y., Iwasawa K. 1998, *AJ*, 115, 460
- Nagao T., Taniguchi Y., Murayama T. 2000, *AJ*, 119, 2605
- Nandra, K., Pounds, K. A. 1994, *MNRAS*, 268, 405
- Neumayer, N., Cappellari, M., Reunanen, J., Rix, H.-W., van der Werf, P. P., de Zeeuw, P. T., Davies, R. I. 2007, *ApJ*, 671, 1329
- Nucita, A. A., Guainazzi, M., Longinotti, A. L., et al. 2010, *A&A*, 515A, 47
- Oke J. B., Sargent W. L. 1968, *ApJ*, 151, 807
- Oliva E., Salvati M., Moorwood A. F. M., Marconi A. 1994, *A&A*, 288, 457

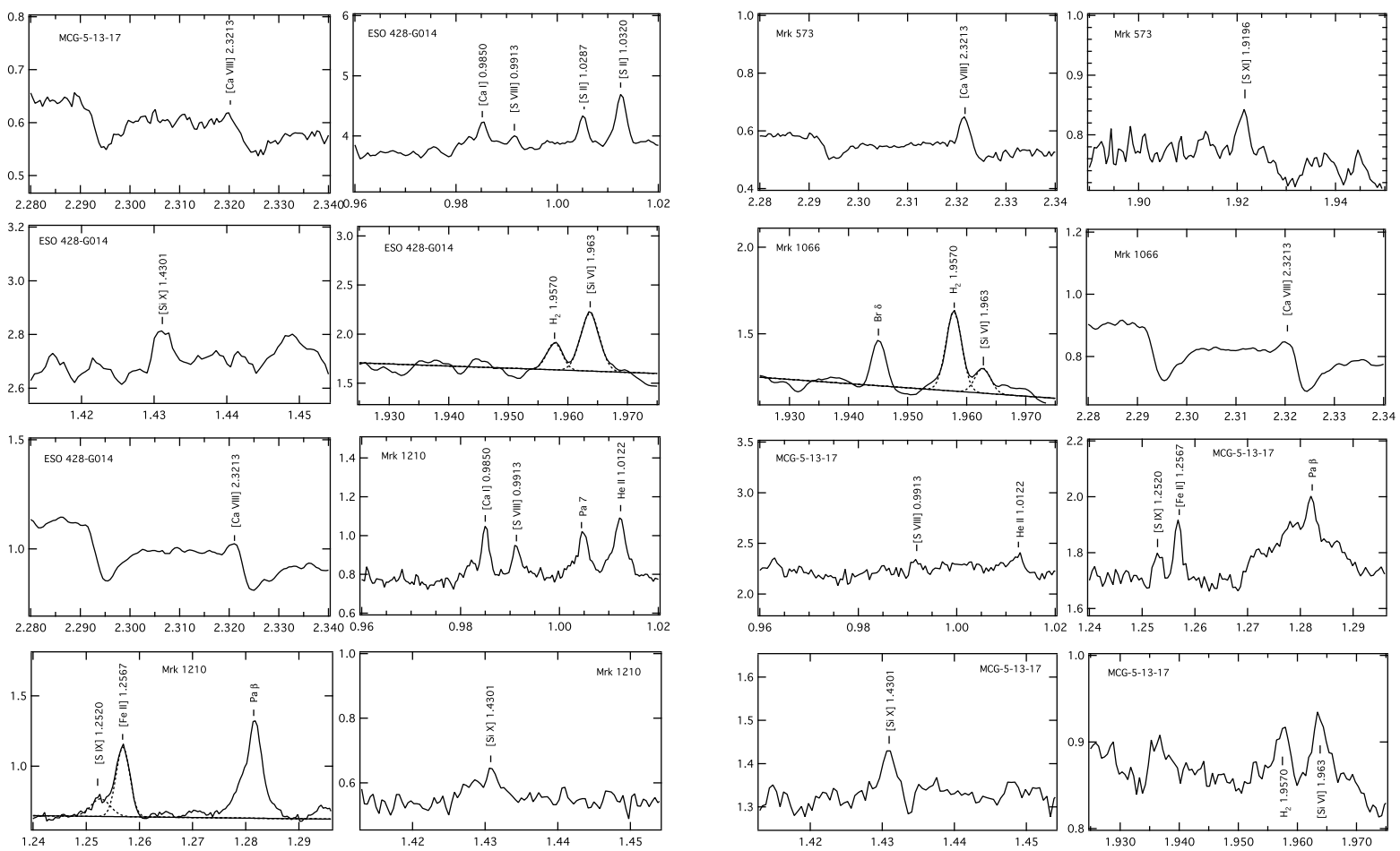
- Oliva E., Marconi A., Moorwood A. F. M. 1999, *A&A*, 342, 87
- Oliva E. et al. 2001, *A&A*, 369, L5
- Osterbrock D. E., Parker R. A. 1964, *ApJ*, 141, 892
- Osterbrock D. E. 1969, *Astrophys. Lett.*, 4, 57
- Osterbrock D. E. 1981, *ApJ*, 246, 696
- Osterbrock D. E., Martel A. 1993, *ApJ*, 414, 552
- Panessa F., Bassani L., Cappi M., Dadina M., Barcons X., Carrera F. J., Ho L. C., Iwasawa K. 2006, *A&A*, 455, 173
- Pelat D., Alloin D., Fosbury R. A. E. 1981, *MNRAS*, 195, 787
- Pelat D., Alloin D., Bica E. 1987, *A&A*, 182, 9
- Penston M. V., Fosbury A. E., Boksenberg A., Ward M. J., Wilson A. S. 1984, *MNRAS*, 208, 347
- Pfefferkorn F., Boller Th., Rafanelli P. 2001, *A&A*, 368, 797
- Pier E. A., Voit G. M. 1995, *ApJ*, 450, 628
- Pogge R. W., Owen J. M. 1993, *Ohio State Uni. Int. Rep.*, 93-01
- Porquet D., Dumont A.M., Collin S., Mouchet M. 1999, *A&A*, 341, 58
- Prieto M. A., Viegas S. M. 2000, *ApJ*, 532, 238
- Prieto M. A, Pérez García A. M., Rodríguez Espinosa J. M. 2002, *MNRAS*, 329, 309
- Prieto M. A., Meisenheimer, K., Marco, O., et al. 2004, *ApJ*, 614, 135
- Prieto M. A, Marco O., Gallimore J. 2005, *MNRAS*, 364, L28
- Ramos-Almeida C., Pérez García A.M., Acosta-Pulido J.A., Rodríguez Espinosa J.M., Barrena R., Manchado A. 2006, *ApJ*, 645, 148
- Reunanen J., Kotilainen J. K., Prieto M. A. 2002, *MNRAS*, 331, 154
- Reunanen J., Kotilainen J. K., Prieto M. A. 2003, *MNRAS*, 343, 192
- Reynolds, C. S. 1997, *MNRAS*, 286, 513

- Riffel R., Rodríguez-Ardila A., Pastoriza M. G. 2006, *A&A*, 457, 61
- Riffel, R., Pastoriza, M. G., Rodríguez-Ardila, A., Bonatto, C. 2009, *MNRAS*, 400, 273
- Rodríguez-Ardila A., Viegas S. M., Pastoriza M., Prato L. 2002, *ApJ*, 579, 214
- Rodríguez-Ardila A., Contini M., Viegas S. M. 2005, *MNRAS*, 357, 220
- Rodríguez-Ardila A., Prieto M. A., Viegas S. M., Gruenwald R. 2006, *ApJ*, 653, 1098
- Rose, M., Tadhunter, C. N., Holt, J., Ramos Almeida, C., Littlefair, S. P. 2011, *MNRAS*, 414, 3360
- Rush B., Malkan M. A., Fink H. H., Voges W. 1996, *ApJ*, 471, 190
- Sambruna, R. M., Brandt, W. N., Chartas, G., Netzer, H., Kaspi, S., et al. 2001, *ApJ*, 546, L9
- Sambruna, R. M., Netzer, H., Kaspi, S., Brandt, W. N., Chartas, G., et al. 2001, *ApJ*, 546, L13
- Shields G. A., Oke J. B. 1975, *ApJ*, 1975
- Shinozaki K., Miyaji T., Ishisaki Y., Ueda Y., Ogasaka Y. 2006, *AJ*, 131, 2843
- Schlesinger, K., Pogge, R. W., Martini, P., Shields, J. C., Fields, D. 2009, *ApJ*, 699, 857
- Shuder J. M. 1980, *ApJ*, 240, 32
- Shuder J. M., Osterbrock D. E. 1981, *ApJ*, 250, 55
- Storchi-Bergmann T., Winge C., Ward M. J., Wilson A. S. 1999, *MNRAS*, 304, 35
- Terashima, Yuichi; Iyomoto, Naoko; Ho, Luis C.; Ptak, Andrew F.
- Thompson R. I. 1995, *ApJ*, 445, 700
- Thompson R. I. 1996, *ApJ*, 459, L61
- Viegas-Aldrovandi S. M., Contini M. 1989, *A&A*, 215, 253
- Walter R., Fink H. H. 1993, *A&A*, 274, 105
- Ward M., Morris S. 1984, *MNRAS*, 207, 867
- Wilson A. S. 1979, *Proc. R. Soc. Lond.*, A366, 461

Whittle, M., Rosario, D. J., Silverman, J. D., Nelson, C. H., Wilson, A. S. 2005, AJ, 129, 104

.

Fig. 2.— Same as Fig. 1 for Mrk 573 (cont.), Mrk 1066, MCG-5-13-17, ESO 428-G014 and Mrk 1210.



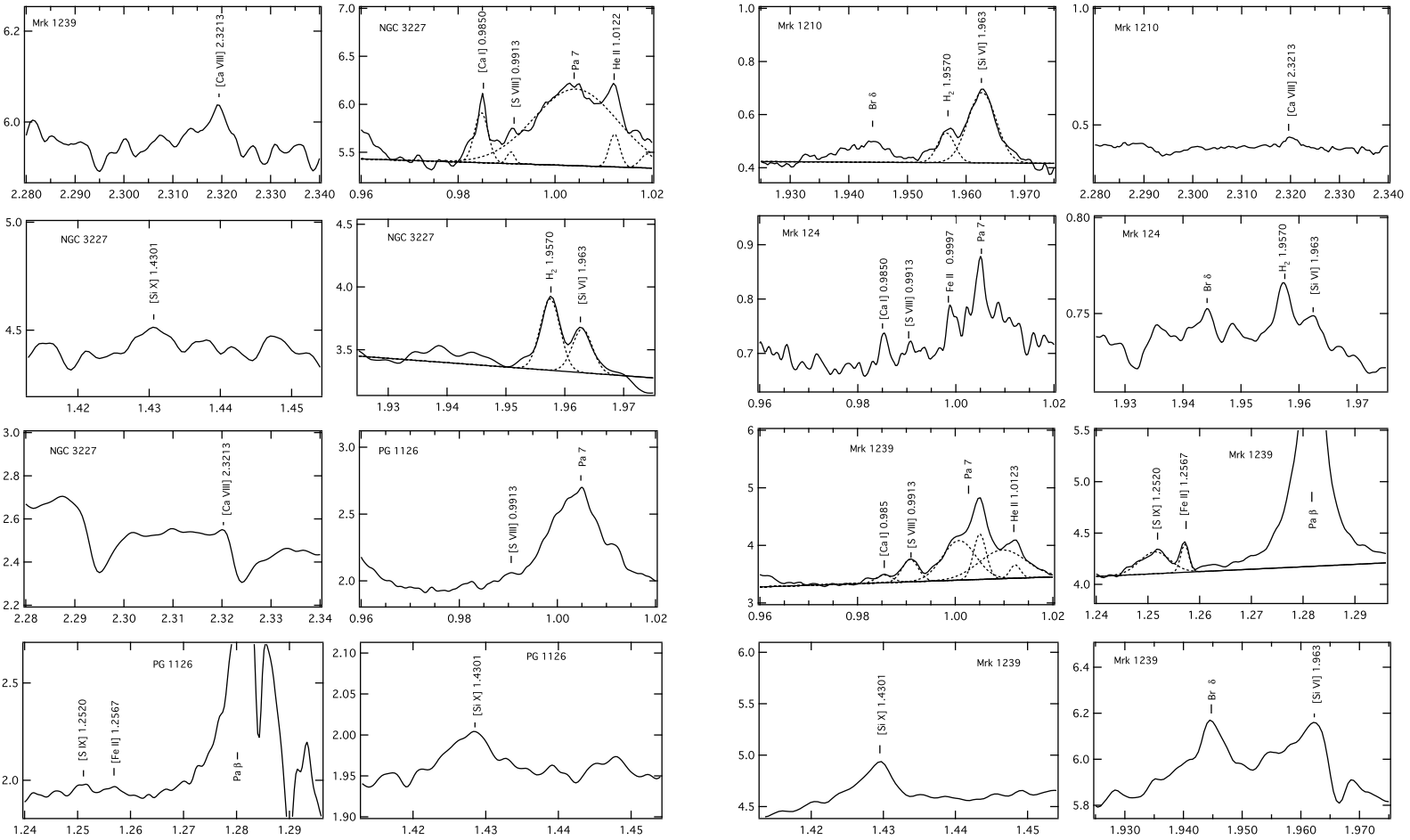


Fig. 3.— Same as Fig. 1 for Mrk 1210 (cont.), Mrk 124, Mrk 1239, NGC 3227 and PG1126-041

Fig. 4.— Same as Fig. 1 for PG 1126-041 (cont.), H 1143-182, NGC 4051 and NGC 4151.

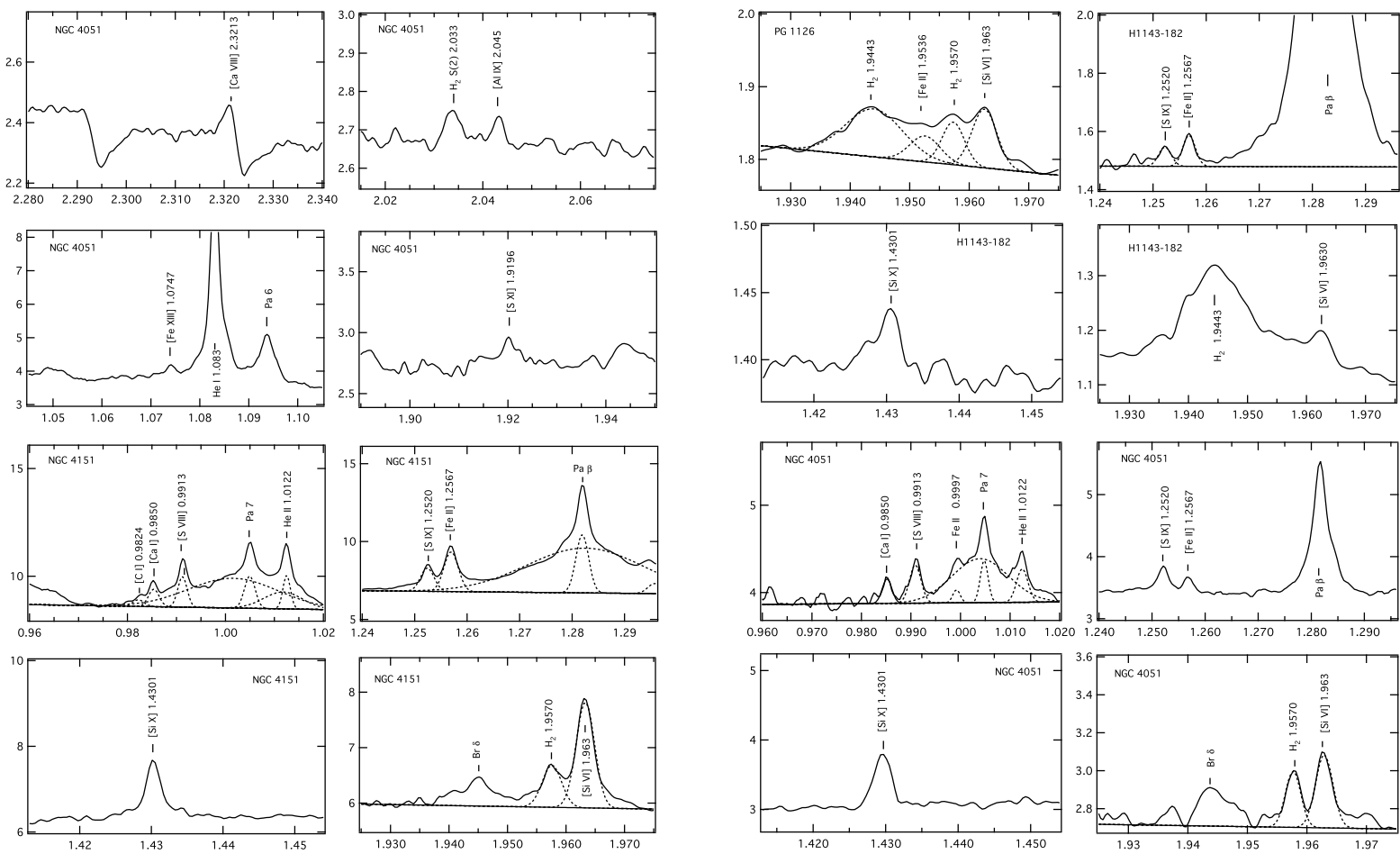


Fig. 5.— Same as Fig. 1 for NGC 4151 (cont.), NGC 4748, Mrk 279, NGC 5548 and NGC 5728.

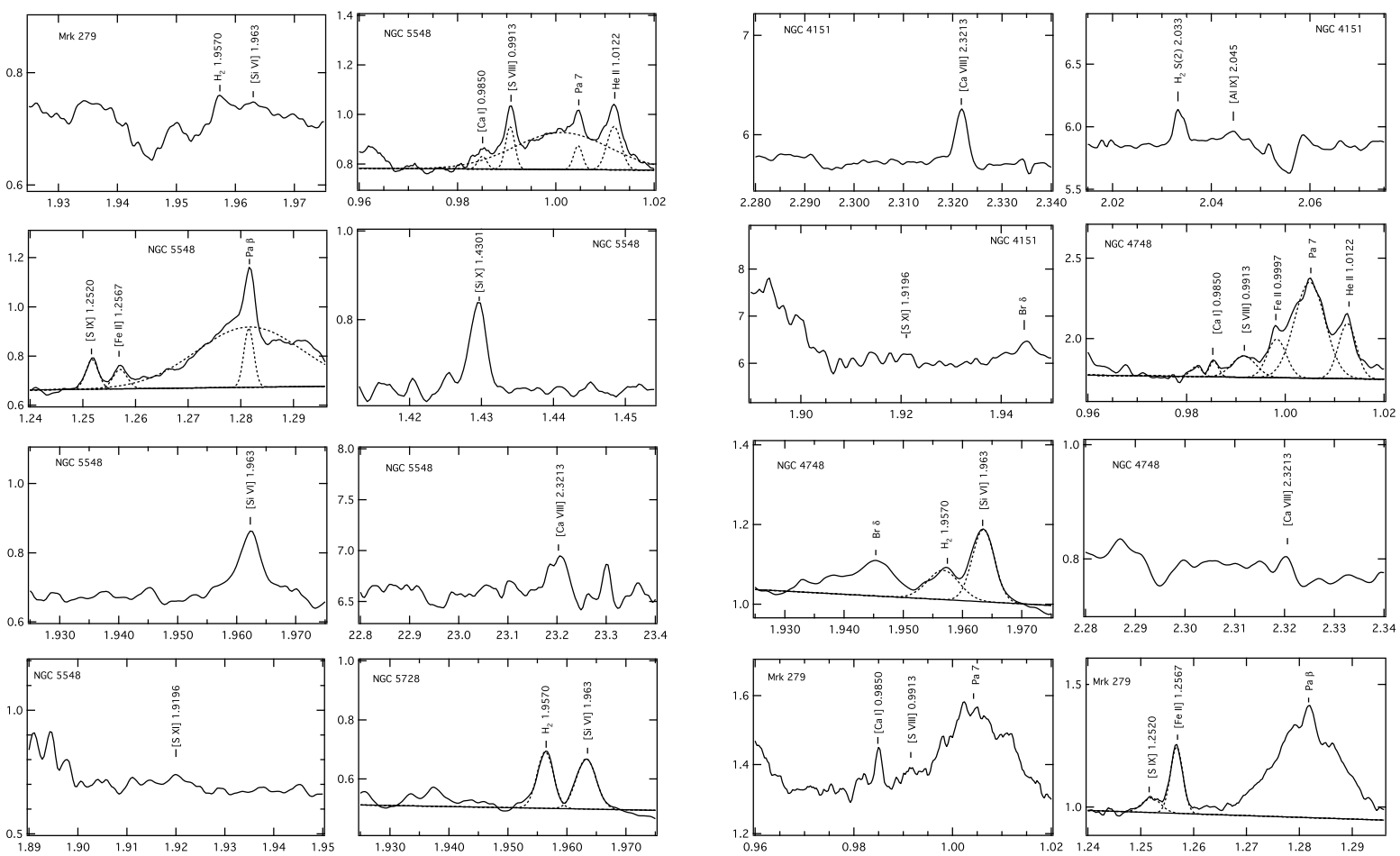


Fig. 6.— Same as Fig. 1 for PG 1448+273, PG 1612+261, Mrk 504, Mrk 509, Mrk 896 and 1H 2107-097.

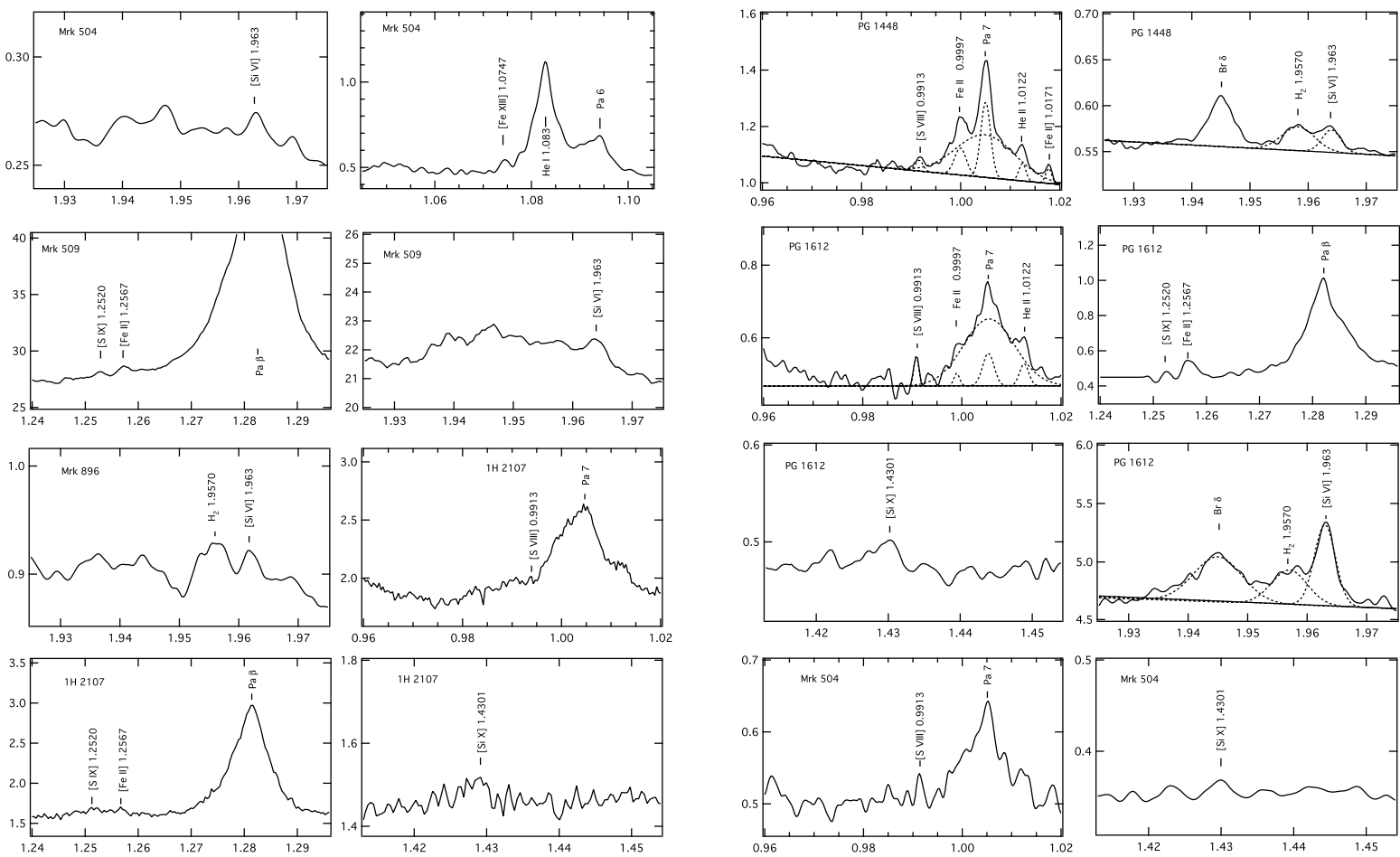
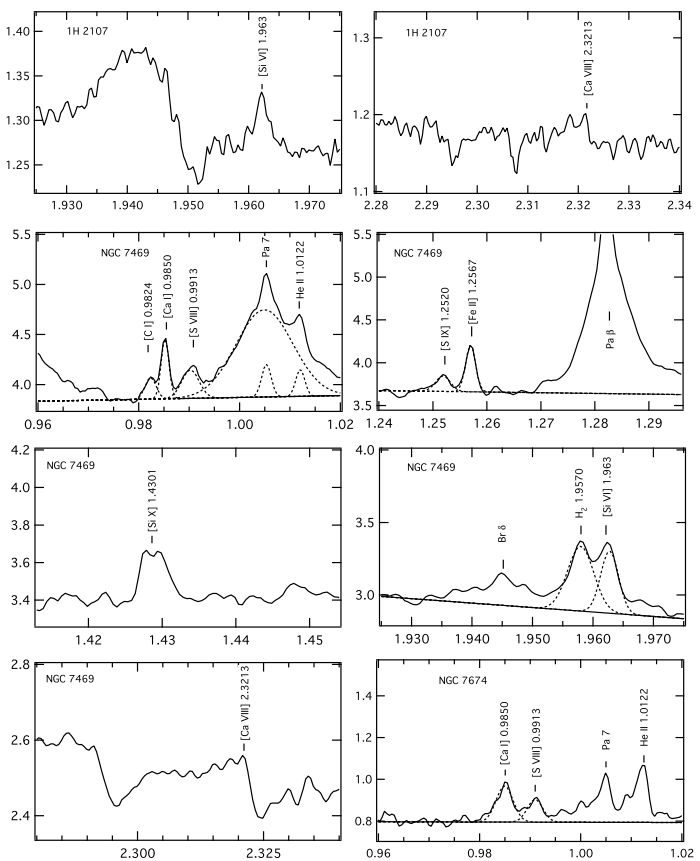
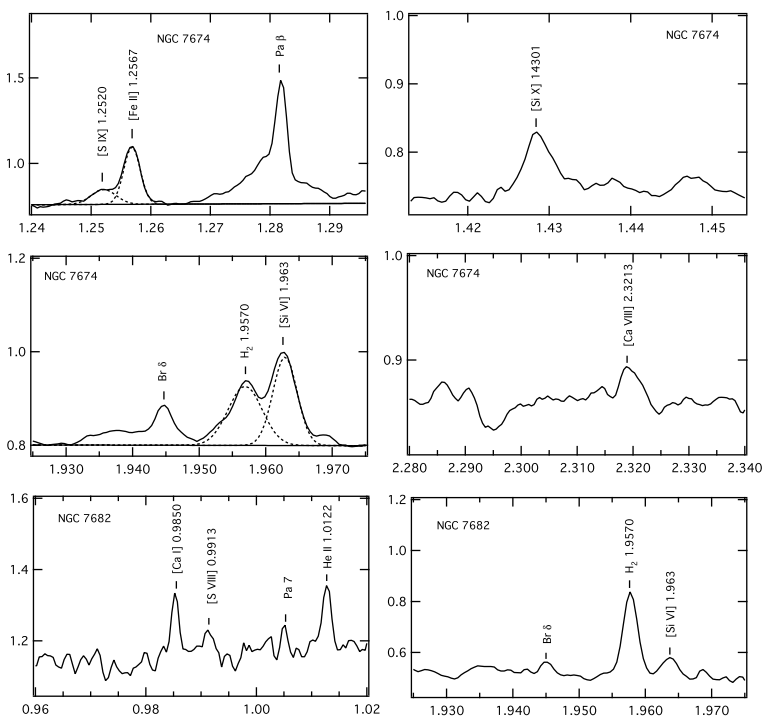


Fig. 7.— Same as Fig. 1 for 1H 2107-097 (cont.), NGC 7469, NGC 7674 and NGC 7682.



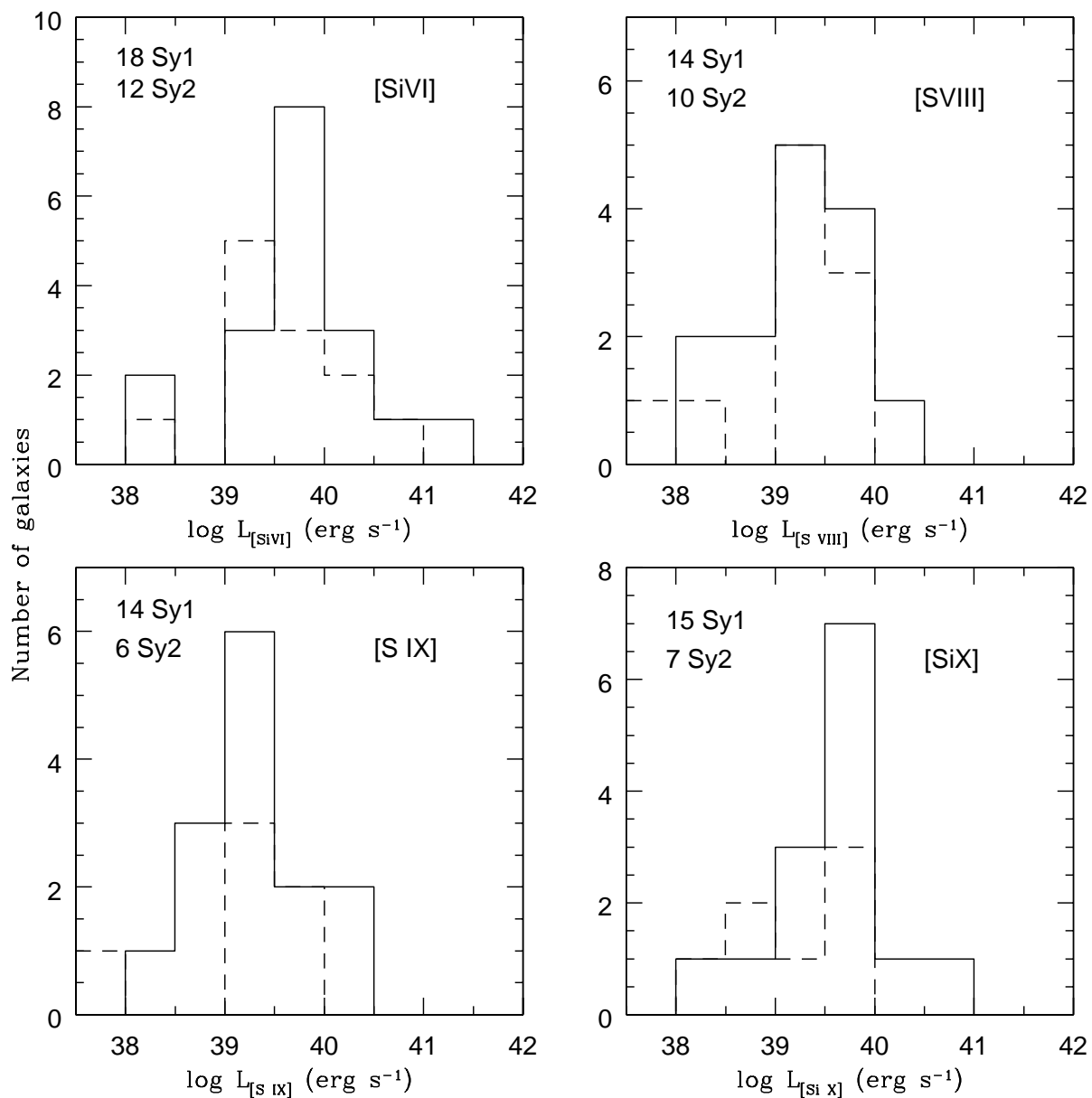


Fig. 8.— Histogram with the number of galaxies for each bin of log in luminosity (full line for Ty1 and dashed line for Ty2 AGNs) for the four most frequent coronal lines found in the sample. The total numbers of Ty1 and Ty2 AGNs used for every line are indicated in the upper left corner of each panel.

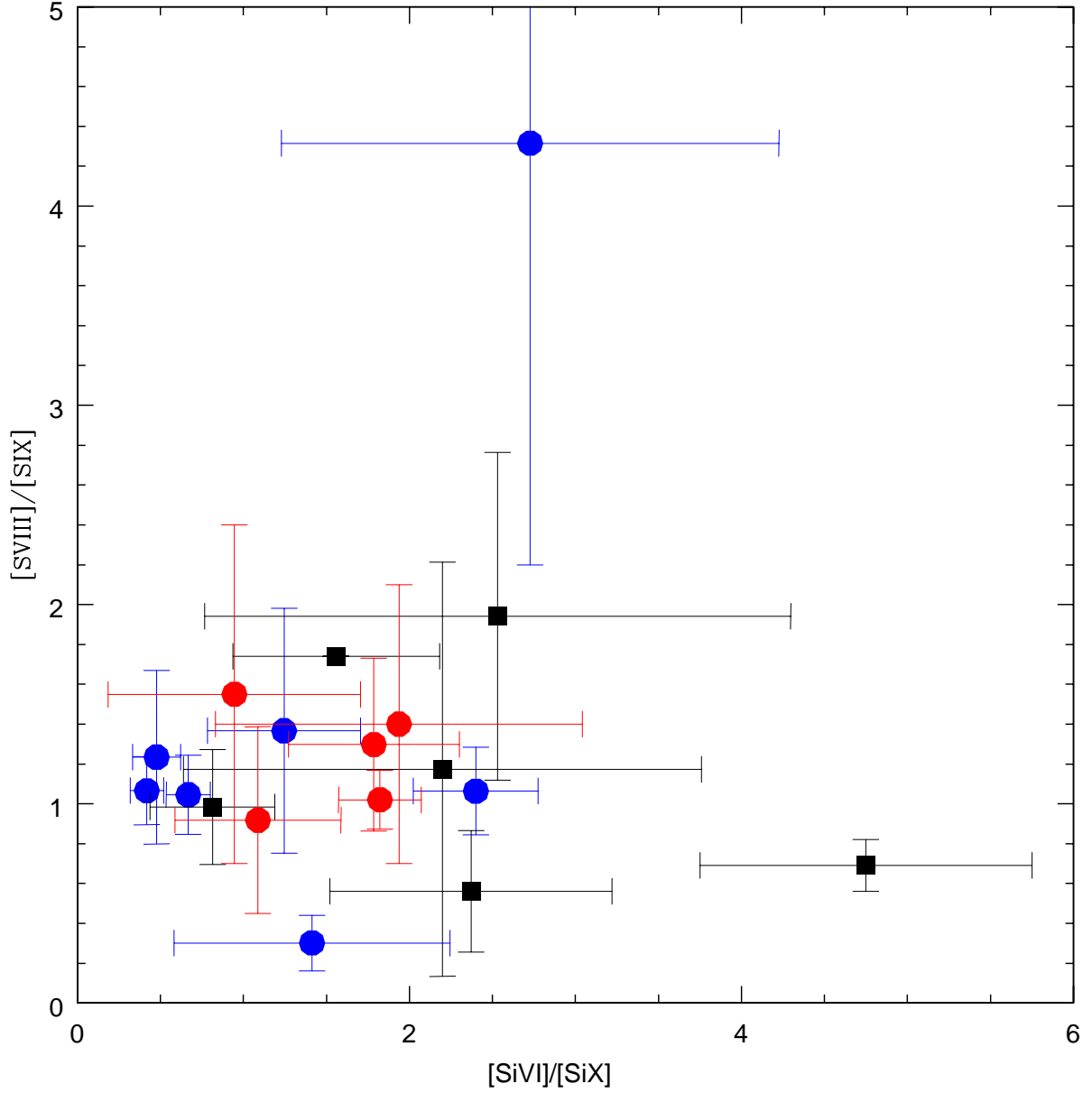


Fig. 9.— Flux ratio $[Si\text{ VI}]/[Si\text{ X}]$ versus $[S\text{ VIII}]/[Si\text{ X}]$ measured for the objects where at least 3 of the fluxes involved was detected at 3σ level. Circles correspond to Ty1s (classical and NLS1) and squares to Ty2 AGNs.

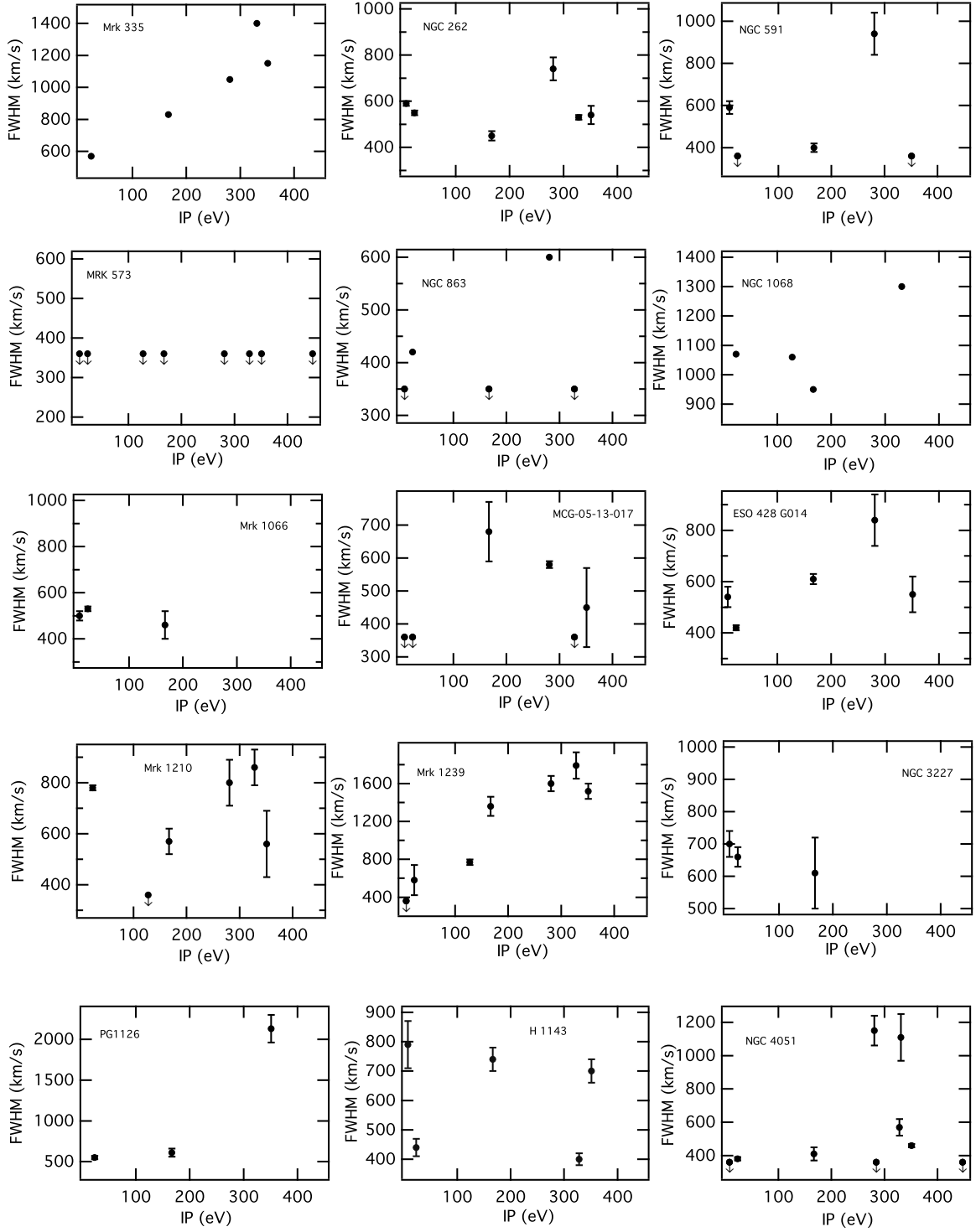


Fig. 10.— The FWHM vs IP for coronal lines detected in each galaxy. FWHM values are corrected for instrumental resolution. For purposes of comparison we include the low-ionization lines [Fe II] 1.2569 μm and [S III] 0.953 μm . Data points lacking error bars were taken from the literature, with no report of uncertainty.

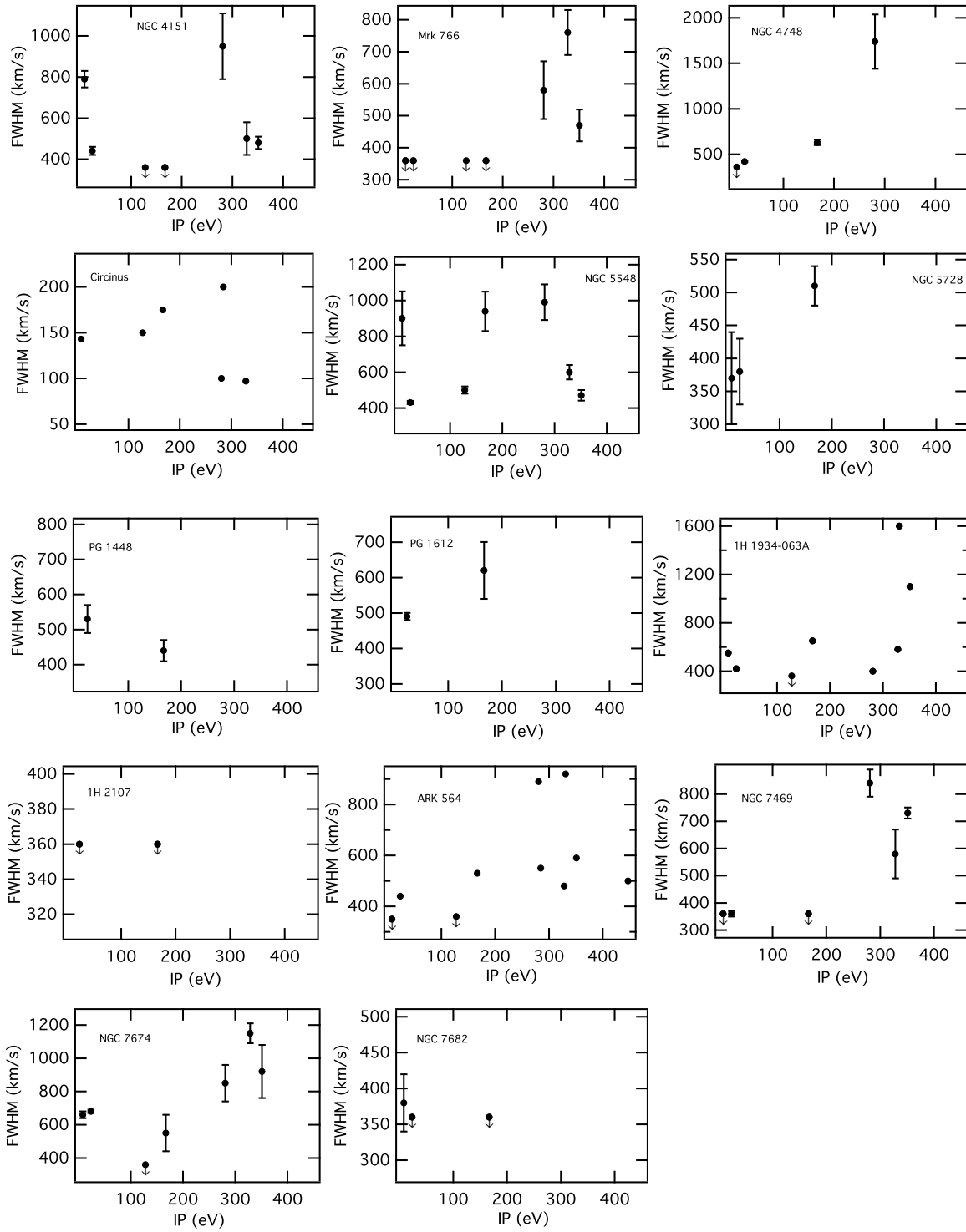


Fig. 11.— Cont. of Fig. 10.

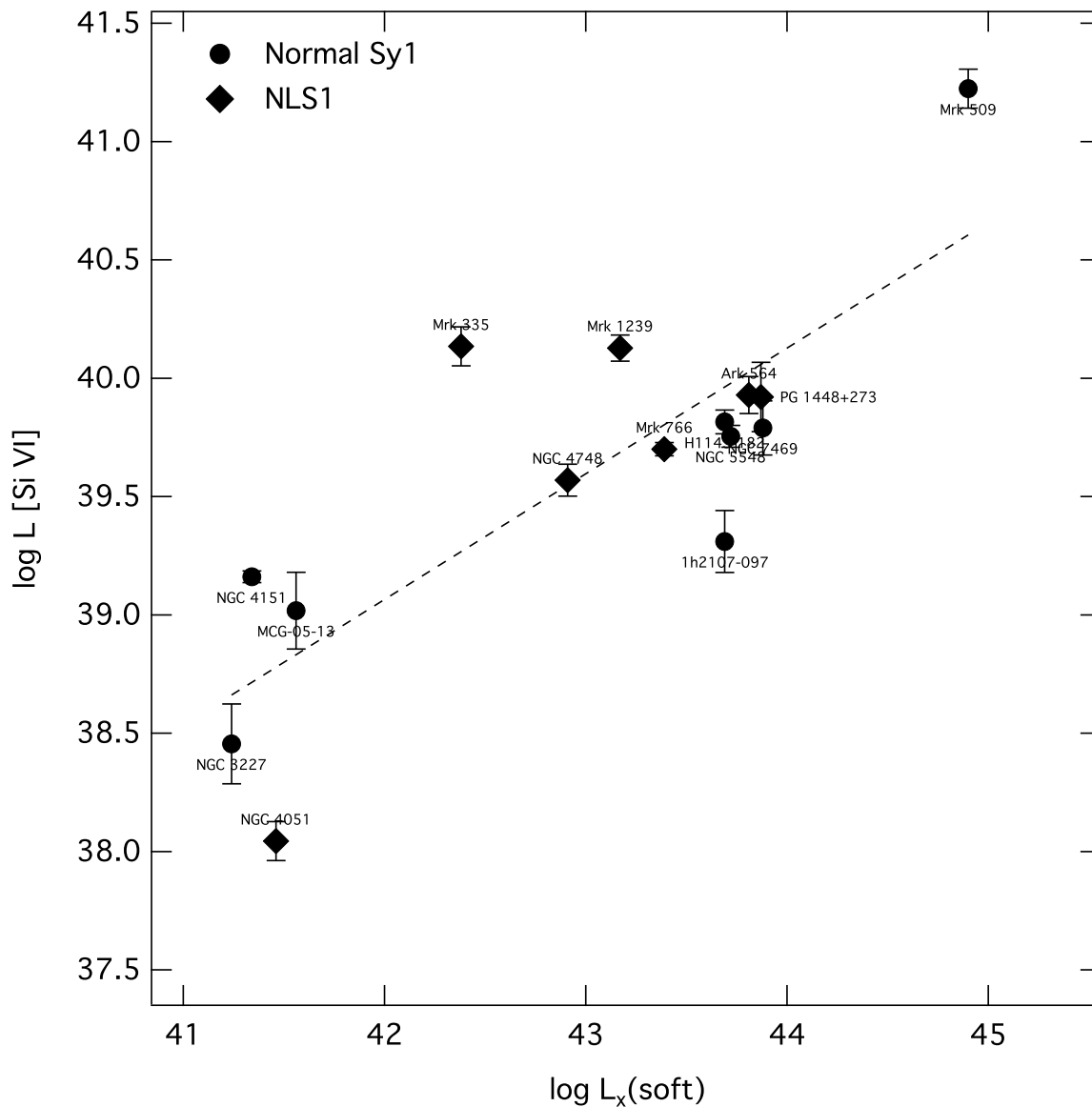


Fig. 12.— Luminosity of [Si VI] 1.963 μm (erg s^{-1}) versus the soft X-ray luminosity (erg s^{-1}). Soft X-ray data are from Pfefferkorn, Boller & Rafanelli (2001) (NGC 3227, NGC 4151, NGC 5548, Mrk 1239, NGC 4051, Mrk 766, NGC 4748, NGC 7469, Mrk 493 and Mrk 335), Rush et al. (1996) (MCG-05-13-017, NGC 7682 and Mrk 509) and Walter & Fink (1993) (Ark 564, PG1448+273 and H1143-182). The dashed line is a linear correlation fitted to the data.

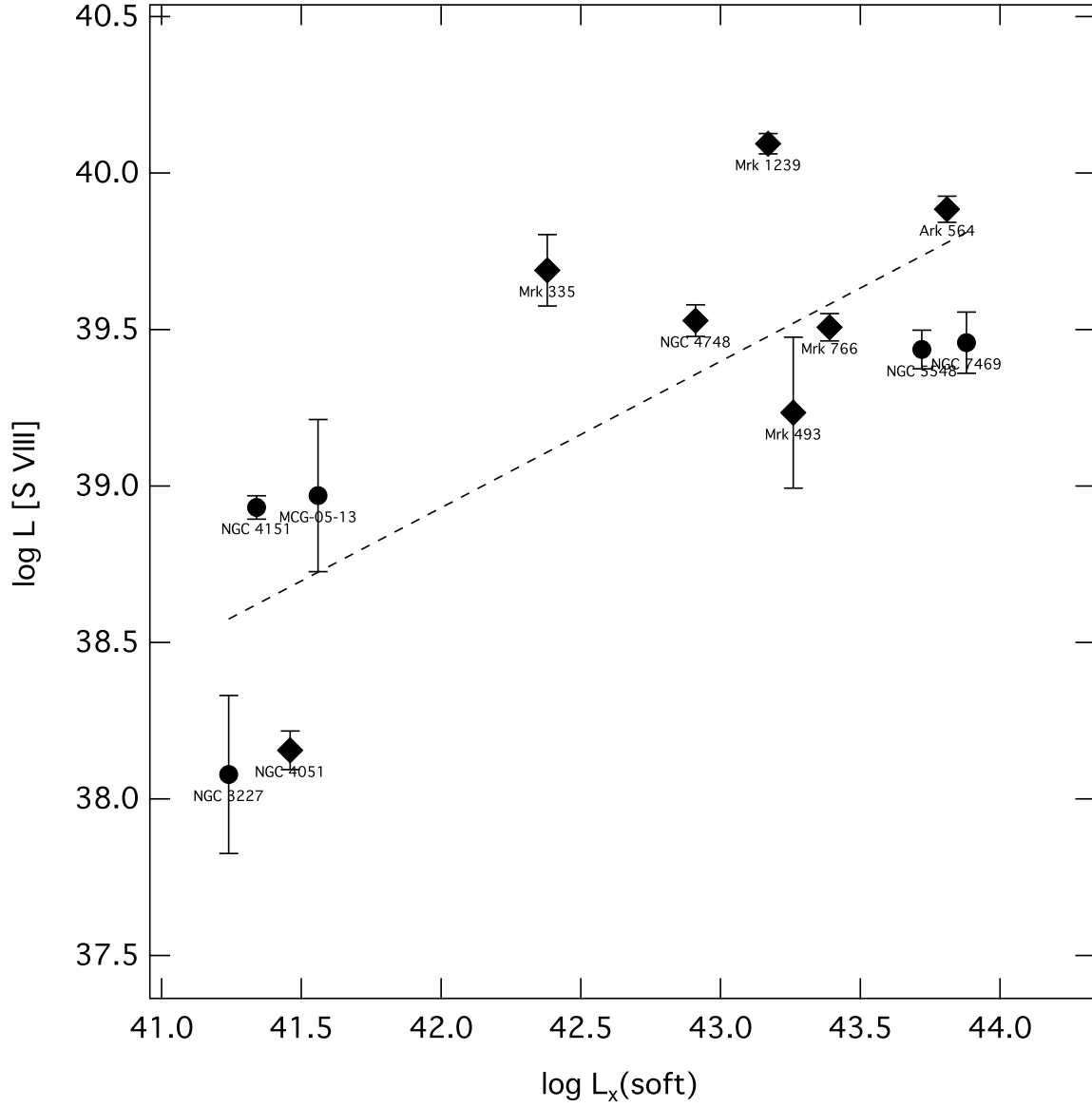


Fig. 13.— Luminosity of [S VIII] 0.991 μm (erg.s⁻¹) vs the soft X-ray luminosity (erg.s⁻¹). Labels and symbols are the same as in figure 12. The dashed line is a linear correlation fitted to the data.

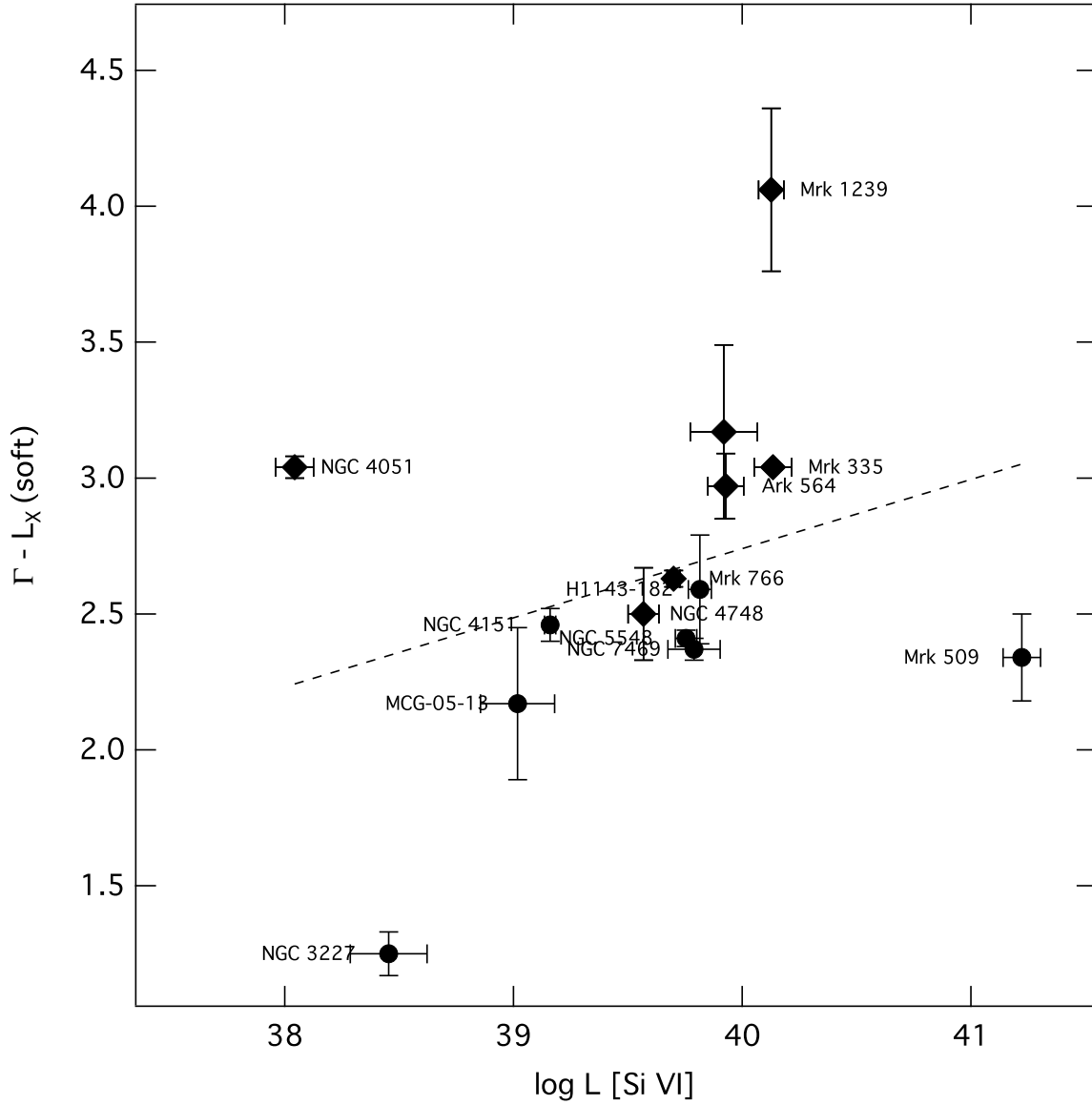


Fig. 14.— Photon index (Γ) of soft X-rays (0.1-2.4 keV) versus luminosity of [Si VI] $1.963 \mu\text{m}$ (erg.s^{-1}). All data of soft X-ray are from Pfefferkorn, Boller & Rafanelli (2001). The dashed line is a linear correlation fitted to the data.

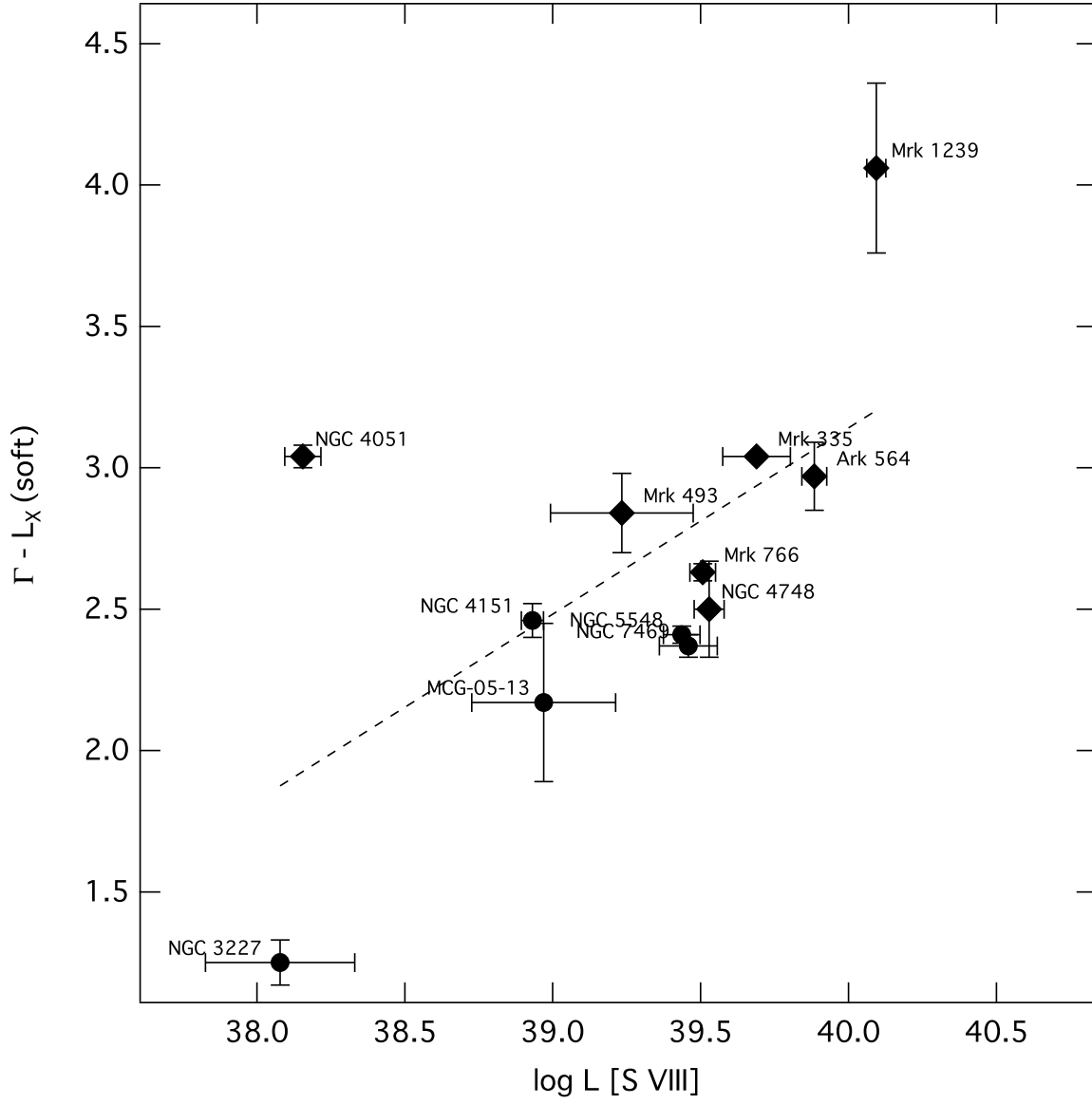


Fig. 15.— Same as in Fig. 14 but now in the abscissa is the luminosity of [S VIII] $0.991 \mu\text{m}$ ($\text{erg}\cdot\text{s}^{-1}$).

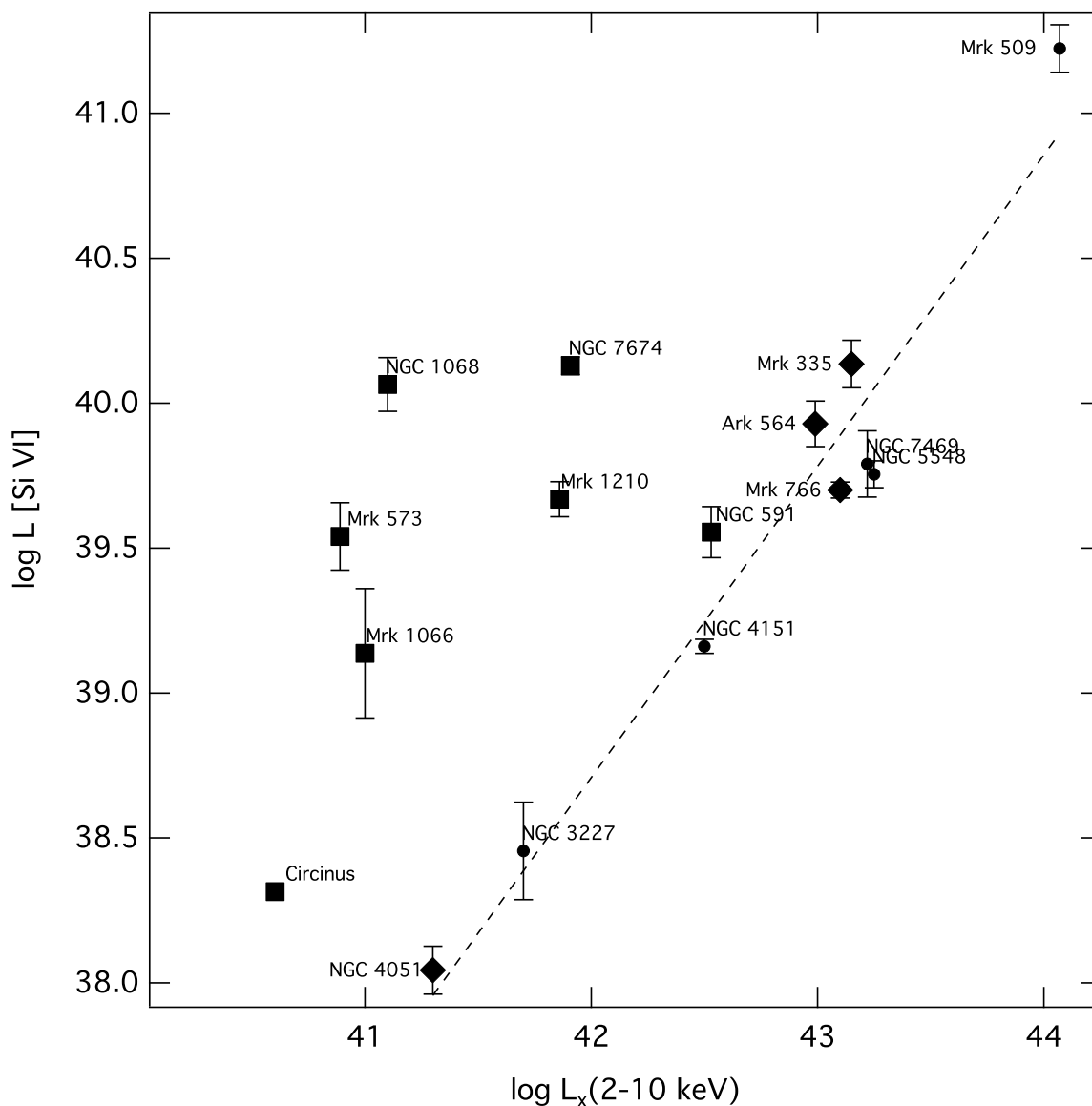


Fig. 16.— Luminosity of [Si VI] 1.963 μm (erg.s⁻¹) versus the hard X-ray luminosity (erg.s⁻¹). Labels have the same meaning as in Fig. 12. Data of hard X-ray are from Cappi et al. (2006) (NGC 3227, NGC 4151, NGC 4051, NGC 1068); Bassani et al. (1999) (NGC 7674, Mrk 1210, Circinus); Kaspi et al. (2005) (NGC 7469, Mrk 509); Guainazzi, Matt & Perola (2005) (Mrk 573, NGC 591); Leighly (1999) (Mrk 335, Mrk 766); Shinozaki et al. (2006) (Ark 564); Levenson, Weaver & Heckman (2001) (Mrk 1066) and Panessa et al. (2006) (NGC 5548). The dashed line is a linear correlation fitted to the data.

Table 1. Galaxy sample. Redshifts were taken from NASA/IPAC Extragalactic Database (NED). The last column indicates if the correspondent galaxy emits at least one coronal line (Y) or none (N) with IP $\gtrsim 100$ eV in its NIR spectrum .

Galaxy	Type	z	"/pc	CL
Mrk 334	Sy1	0.021940	460	N ^a
Mrk 335*	NLS1	0.025785	500	Y
NGC 262	Sy2	0.015034	290	Y
Ton S180*	NLS1	0.061980	1200	N
Mrk 993	Sy2	0.015537	300	Y
NGC 591	Sy2	0.015167	290	Y
Mrk 573	Sy2	0.017179	330	Y
NGC 863*	Sy1	0.026385	550	Y
Mrk 1044*	NLS1	0.016451	320	N
NGC 1068*	Sy2	0.003793	75	Y
NGC 1097	Sy1	0.004240	90	N
NGC 1144	Sy2	0.028847	560	N ^a
Mrk 1066	Sy2	0.012025	230	Y
NGC 1275	Sy2	0.017559	340	N
MCG-05-13-017	Sy1	0.012445	260	Y
NGC 2110	Sy2	0.007789	150	N ^a
ESO 428-G014	Sy2	0.005664	110	Y
Mrk 78*	Sy2	0.037150	720	Y
Mrk 1210	Sy2	0.013496	260	Y
Mrk 124	NLS1	0.056300	1090	Y
Mrk 1239	NLS1	0.019927	380	Y
NGC 3227	Sy1	0.003859	80	Y
PG 1126-041	NLS1	0.060000	1160	Y
H1143-182	Sy1	0.032949	680	Y
NGC 4051	NLS1	0.002336	45	Y
NGC 4151	Sy1	0.003319	70	Y
Mrk 766	NLS1	0.012929	250	Y
NGC 4748	NLS1	0.014630	280	Y
Ton 0156	QSO	0.549000	11400	N
Mrk 279	NLS1	0.030451	590	Y
Circinus*	Sy2	0.001448	30	Y

Table 1—Continued

Galaxy	Type	z	"/pc	CL
NGC 5548	Sy1	0.017175	360	Y
PG 1415+451	Sy1	0.113587	2350	N
Mrk 684	Sy1	0.046079	950	N
Mrk 478	NLS1	0.079055	1530	N
NGC 5728	Sy2	0.009353	180	Y
PG 1448+273	NLS1	0.065000	1250	Y
PG 1519+226	NLS1	0.013700	2650	N
NGC 5929	Sy2	0.008312	160	N ^a
NGC 5953	Sy2	0.006555	130	N
Mrk 291	NLS1	0.035198	680	N
Mrk 493	NLS1	0.031328	610	N ^a
PG 1612+261	Sy1	0.130916	2700	Y
3C 351	QSO	0.371940	7700	N
Mrk 504	NLS1	0.035888	700	Y
Arp 102B	Sy1	0.024167	500	N
1H 1934-063A	NLS1	0.010254	200	Y
Mrk 509	Sy1	0.034397	710	Y
Mrk 896	NLS1	0.026424	510	Y
1H 2107-097	Sy1	0.026525	550	Y
Ark 564	NLS1	0.024684	480	Y
NGC 7469	Sy1	0.016317	340	Y
NGC 7674	Sy2	0.028924	560	Y
NGC 7682	Sy2	0.017140	330	Y

*Data taken from the literature.

^aNo coronal lines were detected in the 0.8–2.4 μm region but other authors have reported coronal lines in other spectral regions. See Sect 2 for further details.

Table 2. Fluxes of the CLs for the galaxy sample in units of 10^{-15} erg cm $^{-2}$ s $^{-1}$. For the recombination lines the fluxes correspond to the narrow component, except when specified.

Galaxy	Pa α 1.8750 μ m	Br γ 2.1654 μ m	[Ca VIII] 2.3213 μ m	[Si VI] 1.9630 μ m	[S VIII] 0.9913 μ m	[Al IX] 2.0450 μ m	[S IX] 1.2520 μ m	[Fe XIII] 1.0747 μ m	[Si X] 1.4301 μ m	[S XI] 1.9196 μ m
Mrk 334	12.6 \pm 0.4	4.7 \pm 0.2	***	< 2.0	< 0.7	< 0.8	< 1.4	< 1.8	< 1.8	< 1.3
Mrk 335	...	26.7 \pm 3.1 \S^a	...	10.6 \pm 2.0 a	3.8 \pm 1.0 a	...	12.6 \pm 2.5 a	18.3 \pm 3.8 a	7.5 \pm 3.0 a	...
NGC 262	35.3 \pm 1.1	1.1 \pm 0.1	< 0.8	4.4 \pm 0.7	2.7 \pm 1.1	< 0.3	2.3 \pm 1.1	< 1.7	2.0 \pm 1.1	< 1.8
Ton S180	...	5.3 \pm 1.0 \S^a	*
Mrk 993	**	...	***	< 2.0	< 0.9	< 0.5	< 1.1	< 1.8	< 1.7	< 1.8
NGC 591	60.1 \pm 0.8	3.6 \pm 0.2	***	8.1 \pm 1.6	3.3 \pm 1.4	< 0.7	< 1.7	< 2.1	3.2 \pm 1.6	< 1.6
Mrk 573	45.5 \pm 0.3	2.8 \pm 0.1	3.2 \pm 0.5	6.1 \pm 1.6	6.1 \pm 0.9	< 0.6	6.2 \pm 0.9	3.3 \pm 1.6	7.5 \pm 1.5	2.2 \pm 1.7
NGC 863	...	9.3 \pm 2.6 \S^a	...	< 2.1 a	< 1.0 a	...	1.1 \pm 0.4 a	...	3.2 \pm 1.0 a	...
Mrk 1044	...	7.8 \pm 1.5 \S^a	**	...
NGC 1068	...	34.6 \pm 4.1 k	450 b	421 \pm 90 c	87 b	...	50 b	...	270 \pm 50 e	...
NGC 1097	**	...	***	< 3.8	< 2.8	< 0.9	< 3.0	< 3.0	< 2.5	**
NGC 1144	***	< 0.9	< 0.6	< 0.2	< 0.4	< 1.2	< 0.5	< 0.8
Mrk 1066	145.7 \pm 1.6	14.2 \pm 0.2	***	4.9 \pm 2.5	< 1.9	< 1.1	< 2.2	< 2.1	< 2.9	< 3.4
NGC 1275	145.1 \pm 2.5	9.8 \pm 0.4	< 1.2	< 1.5	< 1.4	< 0.9	< 2.5	< 1.9	< 1.2	< 0.7
MCG-05-13-017	**	0.8 \pm 0.1 \S	***	3.5 \pm 1.3	3.1 \pm 1.7	< 0.9	2.0 \pm 1.6	< 1.5	3.7 \pm 1.6	< 1.7
NGC 2110	33.0 \pm 4.5	2.5 \pm 0.2	< 0.6	< 0.6	< 1.1	< 0.9	< 1.0	< 4.0	< 5.0	< 1.6
ESO 428-G014	102.1 \pm 0.8	9.0 \pm 0.1	***	21.1 \pm 3.9	4.0 \pm 2.8	< 1.8	< 3.8	< 3.8	4.2 \pm 2.2	< 3.7
Mrk 78	17.5 \pm 2.5 f	2.5 \pm 0.2 f	...	19.7 \pm 1.7 f	1.7 \pm 0.3 f
Mrk 1210	57.2 \pm 1.4	4.6 \pm 0.2 g	1.6 \pm 0.1 g	13.3 \pm 0.9 g	2.9 \pm 0.2 g	< 0.5	4.2 \pm 0.5 g	< 1.8	2.8 \pm 0.4 g	< 2.7
Mrk 124	15.2 \pm 0.5	2.5 \pm 0.6 \S	*	< 0.4	< 0.5	< 0.4	< 0.8	< 2.1	< 0.7	< 0.3
Mrk 1239	50.5 \pm 2.7	14.0 \pm 2.1	5.7 \pm 1.3	17.5 \pm 2.2	16.2 \pm 1.2	< 1.1	15.5 \pm 1.8	< 3.5	26.2 \pm 1.9	< 2.8
NGC 3227	71.7 \pm 2.8	6.5 \pm 1.3	< 0.9	10.0 \pm 3.9	4.2 \pm 2.4	< 1.1	< 2.2	< 2.6	< 3.9	< 3.4
PG 1126-041	32.8 \pm 1.1	13.3 \pm 0.7 \S	*	4.1 \pm 0.4	< 0.8	< 0.5	< 1.3	< 2.8	5.1 \pm 0.7	< 0.8
H1143-182	106.6 \pm 1.4	10.96 \pm 0.7	< 0.9	3.1 \pm 3.6	< 1.4	< 0.2	1.0 \pm 0.5	< 1.1	1.6 \pm 0.5	< 0.4
NGC 4051	111.5 \pm 4.3 \S	13.1 \pm 0.9 \S	2.4 \pm 0.9	10.6 \pm 2.0	13.7 \pm 2.0	1.8 \pm 1.1	11.1 \pm 2.3	8.0 \pm 2.2	22.2 \pm 2.5	5.9 \pm 1.7
NGC 4151	581.5 \pm 12.0 \S^*	12.4 \pm 0.6	15.1 \pm 2.3	68.7 \pm 3.9	40.5 \pm 3.5	2.3 \pm 1.6	39.7 \pm 2.3	< 1.6	37.7 \pm 3.0	< 10.6
Mrk 766	27.2 \pm 0.5 h	7.4 \pm 0.4 h	2.5 \pm 0.6 h	15.6 \pm 1.0 h	10.0 \pm 1.0 h	...	9.4 \pm 1.0 h	...	6.5 \pm 0.6 h	...
NGC 4748	43.2 \pm 0.6	1.4 \pm 0.1	< 1.4	9.0 \pm 1.4	8.2 \pm 1.0	< 0.8	1.9 \pm 0.7	< 1.6	3.3 \pm 1.3	< 1.4
Ton 0156	*	*	*	*	< 0.2	...	< 0.4	< 0.4	< 0.1	*
Mrk 279	17.5 \pm 0.5 \S^*	0.6 \pm 0.4	< 0.8	< 0.8	< 0.5	< 0.4	< 0.7	2.9 \pm 1.1	**	< 1.1
Circinus	...	14.1 i	48 \S^i	51.5 \S^i	11 j	10.8 \S^i	20 j
NGC 5548	**	16.3 \pm 2.0 \S	1.7 \pm 0.8	10.0 \pm 1.1	4.8 \pm 0.7	< 0.3	3.7 \pm 0.7	< 0.6	5.6 \pm 1.0	1.5 \pm 1.2
PG 1415+561	21.4 \pm 0.7 \S	...	*	< 0.2	< 0.4	< 0.1	**	< 0.4	< 0.5	< 0.2
Mrk 684	24.3 \pm 0.5	4.5 \pm 0.5 \S	*	< 0.6	< 0.9	< 0.4	< 0.5	< 3.6	< 0.5	< 0.7

Table 2—Continued

Galaxy	Pa α 1.8750 μm	Br γ 2.1654 μm	[Ca VIII] 2.3213 μm	[Si VI] 1.9630 μm	[S VIII] 0.9913 μm	[Al IX] 2.0450 μm	[S IX] 1.2520 μm	[Fe XIII] 1.0747 μm	[Si X] 1.4301 μm	[S XI] 1.9196 μm
Mrk 478	31.2 ± 0.6	7.0 ± 0.6 [§]	*	< 0.3	< 0.8	< 0.4	< 1.4	< 1.4	< 0.7	< 0.3
NGC 5728	20.6 ± 1.9	2.1 ± 0.2	< 0.9	7.1 ± 1.8	< 1.7	< 0.5	< 2.0	< 2.9	< 1.2	< 0.6
PG 1448+273	27.0 ± 1.2	1.5 ± 0.2	*	1.0 ± 0.3	< 0.8	< 0.2	< 1.1	< 0.8	< 0.3	< 0.3
PG 1519+226	9.8 ± 0.4	*	*	< 0.2	< 0.6	< 0.1	< 0.6	< 0.5	< 0.4	< 0.2
NGC 5929	**	1.4 ± 0.3	< 0.5	< 0.9	< 1.0	< 0.4	< 0.9	< 2.1	< 3.0	< 5.6
NGC 5953	19.3 ± 0.8	...	***	< 3.8	< 1.3	< 1.1	< 3.4	< 3.4	< 3.8	< 2.6
Mrk 291	9.4 ± 0.2	0.4 ± 0.1	***	< 1.7	< 0.3	< 0.2	< 0.5	< 1.0	< 0.5	< 0.1
Mrk 493	23.8 ± 0.5	1.8 ± 0.3	< 0.5	< 0.4	0.9 ± 0.5	< 0.5	1.4 ± 0.8	< 0.8	< 0.9	< 0.4
PG 1612+261	13.2 ± 0.2	*	*	2.4 ± 0.4	< 0.8	< 0.3	< 0.7	< 0.4	< 0.6	< 0.3
3C 351	*	*	*	*	**	*	< 1.0	< 2.0	< 1.1	*
Mrk 504	9.6 ± 0.4	3.4 ± 0.5 [§]	< 0.2	< 0.2	0.5 ± 0.3	< 0.1	< 0.6	2.2 ± 0.8	< 0.6	< 0.1
Arp 102B	7.1 [§] *	...	< 0.5	< 0.9	< 0.5	< 0.3	< 1.2	< 1.6	< 1.1	< 0.8
1H 1934-063A	55.0 ± 2.5	22.4 ± 0.1 [§] ^a	3.9 ± 1.1 ^a	24.9 ± 2.5 ^a	12.3 ± 2.8 ^a	...	9.0 ± 2.0 ^a	29.2 ± 4.0 ^a	20.0 ± 5.4 ^a	...
Mrk 509	1422.9 ± 52.1	382.0 ± 33.3 [§]	< 7.8	72.7 ± 13.8	< 11.9	< 6.8	< 8.2	< 12.9	**	< 16.3
Mrk 896	2.7 ± 0.3	0.4 ± 0.1	< 0.6	< 0.7	< 0.8	< 0.2	< 0.6	< 1.0	< 0.7	< 0.7
1H 2107-097	71.7 ± 2.0 [*]	20.9 ± 1.9 [§]	1.4 ± 0.4	1.5 ± 0.4	< 1.8	< 0.3	< 1.2	29.2 ± 2.3	2.3 ± 0.9	< 0.6
Ark 564	62.2 ± 0.8	10.5 ± 0.6 [§] ^a	3.1 ± 1.0 ^a	7.2 ± 1.3 ^a	6.5 ± 0.4 ^a	2.2 ± 0.5	6.1 ± 0.6	5.5 ± 2.9 [†]	17.2 ± 1.0 ^a	3.5 ± 0.5
NGC 7469	25.8 ± 1.6	4.5 ± 0.3	< 1.1	12.4 ± 3.2	5.6 ± 1.3	< 0.7	6.1 ± 1.7	< 1.1	11.4 ± 2.3	< 1.9
NGC 7674	32.1 ± 1.1	3.1 ± 0.3	1.5 ± 0.2	8.3 ± 0.6	2.3 ± 0.8	< 3.0	4.1 ± 0.8	< 1.4	3.5 ± 1.0	< 0.7
NGC 7682	31.8 ± 0.8	1.9 ± 0.1	< 0.8	3.0 ± 1.4	2.0 ± 1.0	< 0.4	< 1.5	< 1.8	< 1.4	< 1.5

*Out of the spectral range

**Fall within a telluric zone

***Fall in a CO band absorption zone

[§]Sum of narrow and broad components^{*}Severely affected by atmospheric absorption

References. — ^a Rodríguez-Ardila et al. (2002), ^b Marconi et al. (1996), ^c Rodríguez-Ardila et al. (2006), ^d Oliva et al. (2001), ^e Thompson (1996), ^f Ramos-Almeida et al. (2006), ^g Mazzalay & Rodríguez-Ardila (2007), ^h Rodríguez-Ardila, Contini & Viegas (2005), ⁱ Müeller Sánchez et al. (2006), ^j Oliva et al. (1994), ^k Reunanen, Kotilainen & Prieto (2003), ^l Maiolino et al. (1998)

Table 3. Wavelengths, ionization Potential and critical densities for the studied CLs*. Values for [S III] and [Fe II] are included for purposes of comparison.

Line	λ (μm)	χ , IP (eV)	$\log n_e$ (cm^{-3})	Line	λ (μm)	χ , IP (eV)	$\log n_e$ (cm^{-3})
[S III]	0.9530	23.3	5.8	[Si X]	1.4301	351.1	8.8
[S VIII]	0.9913	280.9	10.6	[S XI]	1.9196	447.1	8.5
[Fe XIII]	1.0747	330.8	8.8	[Si VI]	1.9630	166.8	8.8
[S IX]	1.2520	328.2	9.4	[Al IX]	2.0450	284.6	8.3
[Fe II]	1.2570	7.9	5.0	[Ca VIII]	2.3213	127.7	7.9

*Other most important CLs in the optical and NIR referred to in this work: [Si VII] $2.48\mu\text{m}$, IP=205 eV; [Fe VII] 6087 \AA IP=100 eV; [Fe X] 6374 \AA IP=235 eV; [Fe XI] 7889 \AA IP=262 eV

Table 4. FWHM (in km s^{-1}) of coronal and low-ionization lines in the spectral window $0.8\text{--}2.4 \mu\text{m}$ sorted by increasing value of IP. All data are from the sample of RRAP06 except when indicated. All values of FWHMs are instrument corrected ($\sim 360 \text{ km s}^{-1}$) except when taken from the literature. The last column (T) indicates the general observed trend between FWHM and the ionization potential (three or more data were required): I (increase trend), P (increase trend up to 300 eV and then a decrease or constant), L (level-off), N (no trend).

Galaxy	[Fe II] 1.257 μm	[S III] 0.953 μm	[Ca VIII] 2.3213 μm	[Si VI] 1.9630 μm	[S VIII] 0.9913 μm	[Al IX] 2.0450 μm	[S IX] 1.2520 μm	[Fe XIII] 1.0747 μm	[Si X] 1.4301 μm	[S XI] 1.9196 μm	T
Mrk 335	...	570 ^a	...	830 ^a	1050 ^a	...	†	1400 ^a	1150 ^a	...	P
NGC 262	590 ± 10	550 ± 10	†	450 ± 20	740 ± 50	...	530 ± 10	...	540 ± 40	...	L
Mrk 993	530 ± 30	850 ± 40	...	†	†	
NGC 591	590 ± 30	≤ 360	†	400 ± 20	940 ± 100	≤ 360	†	N
Mrk 573	≤ 360	≤ 360	≤ 360	≤ 360	≤ 360	...	≤ 360	...	≤ 360	≤ 360	
NGC 863	350 ^a	420 ^a	...	350 ^a	600 ^a	...	350 ^a	...	†	...	P
NGC 1068	1070 ^e	‡	1060 ^f	950 ^b	‡	...	‡	1300 ^e	‡	...	N
Mrk 1066	500 ± 20	530 ± 10	†	460 ± 60	L
MCG-05-13-017	≤ 360	≤ 360	†	680 ± 90	580 ± 10	...	≤ 360	...	450 ± 120	...	N
ESO 428-G014	540 ± 40	420 ± 10	†	610 ± 20	840 ± 100	550 ± 70	...	N
Mrk 78	‡	‡	
Mrk 1210	...	780 ± 10	≤ 360	570 ± 50	800 ± 90	...	860 ± 70	...	560 ± 130	...	N
Mrk 124	990 ± 160	550 ± 30	...	†	†	
Mrk 1239	≤ 360	580 ± 160	770 ± 30	1360 ± 100	1600 ± 80	...	1790 ± 140	...	1520 ± 80	...	P
NGC 3227	700 ± 40	660 ± 30	†	610 ± 110	†	†	...	L
PG 1126-041	...	550 ± 20	††	610 ± 10	†	...	†	...	2130 ± 170	...	I
H1143-182	790 ± 80	440 ± 30	...	740 ± 40	400 ± 20	...	700 ± 40	...	N
NGC 4051	≤ 360	380 ± 10	†††	410 ± 40	1150 ± 90	≤ 360	570 ± 50	1110 ± 140	460 ± 10	≤ 360	P
NGC 4151	790 ± 40	440 ± 20	≤ 360	≤ 360	950 ± 160	†	500 ± 80	...	480 ± 30	†	N
Mrk 766	≤ 360	≤ 360	≤ 360	≤ 360	580 ± 90	...	760 ± 70	...	470 ± 50	...	P
NGC 4748	≤ 360	420 ± 10	†	630 ± 30	1740 ± 300	I
Mrk 279	580 ± 30	850 ± 30	...	†	†	...	†	
Circinus	143 ^d	‡	150-540 ^{*h}	175-300 ^{*h}	≤ 100 ^g	200-300 ^{*h}	97 ^d	P
NGC 5548	900 ± 150	430 ± 10	500 ± 20	940 ± 110	990 ± 100	...	600 ± 40	...	470 ± 30	†	N
NGC 5728	370 ± 70	380 ± 50	...	510 ± 40	I
PG 1448+273	...	530 ± 40	††	440 ± 30	†	
PG 1612+261	†††	490 ± 10	††	620 ± 80	†	...	†	...	†	...	
Mrk 504	...	400 ± 30	...	†	†	†	†	...	
1H 1934-063A	550 ^a	420 ^a	350 ^a	650 ^a	400 ^a	...	580 ^a	1600 ^a	1100 ^a	...	P
Mrk 509	500±30	†	...	§	...	
Mrk 896	...	≤ 360	...	†	
1H 2107-097	...	≤ 360	†	≤ 360	†	...	†	...	†	...	
Ark 564	350 ^a	440 ^a	350 ^a	530 ^a	890 ^a	550 ± 20	480 ^a	920 ^a	590 ^a	500 ± 20	P
NGC 7469	≤ 360	360 ± 10	†††	≤ 360	840 ± 50	...	580 ± 90	...	730 ± 20	...	P

Table 4—Continued

Galaxy	[Fe II] 1.257 μm	[S III] 0.953 μm	[Ca VIII] 2.3213 μm	[Si VI] 1.9630 μm	[S VIII] 0.9913 μm	[Al IX] 2.0450 μm	[S IX] 1.2520 μm	[Fe XIII] 1.0747 μm	[Si X] 1.4301 μm	[S XI] 1.9196 μm	T
NGC 7674	660 ± 20	680 ± 10	≤ 360	550 ± 110	850 ± 110	...	1150 ± 60	...	920 ± 160	...	N
NGC 7682	380 ± 40	≤ 360	...	≤ 360	†	L

*Decomposition in two components

†Strongly blended or difficult to measure

††Out of the spectral range

†††Severely affected by intrinsic or atmospheric absorption

‡FWHM is not reported although the line exists

§Fall within a telluric zone

References. — ^a Rodríguez-Ardila et al. (2002), ^b Rodríguez-Ardila et al. (2006), ^c Marconi et al. (1996), ^d Storchi-Bergmann et al. (1999),
^e Alexander, Young & Hough (1999), ^f Reunanen, Kotilainen & Prieto (2003), ^g Oliva et al. (1994), ^h Müller Sánchez et al. (2006)